Miner Deposita (2006) 41: 127–151
DOI 10.1007/s00126-005-0045-3

ARTICLE

Andrew G. Conly · Georges Beaudoin · Steven D. Scott

Isotopic constraints on fluid evolution and precipitation mechanisms for the Boléo Cu–Co–Zn district, Mexico

Received: 10 April 2003 / Accepted: 3 December 2005 / Published online: 30 March 2006

Abstract Stable and radiogenic isotope composition of stratiform Cu–Co–Zn mineralization and associated sedimentary rocks within the Boléo district of the Miocene Santa Rosalía basin, Baja California Sur, constrains the evolution of seawater and hydrothermal fluids and the mechanisms responsible for sulfide and oxide deposition. Stable isotope geochemistry of limestone and evaporite units indicates a strong paleogeographic influence on the chemistry of the water column. Near-shore limestone at the base of the Boléo Formation is characterized by modified marine carbon ($\delta^{13}C_{PDB}$=−6.0 to +4.4‰) and oxygen ($\delta^{18}O_{SMOW}$=+19.5 to +26.2‰) isotope composition due to the influx of ^{13}C- and ^{18}O-depleted fluvial water. Sulfate sulfur isotope composition ($\delta^{34}S_{CDT}$=+17.21 to +22.3‰ and $\delta^{18}O_{SMOW}$=+10.7 to +13.1‰) for basal evaporite and claystone facies are similar to Miocene seawater. Strontium isotopes are less radiogenic than expected for Miocene seawater due to interaction with volcanic rocks. Low S/C ratios, high Mn contents and sedimentological evidence indicate the basin water column was oxidizing. The oxygenated basin restricted sulfide precipitation to within the sedimentary pile by replacement of early diagenetic framboidal pyrite and pore-space filling by Cu–Co–Zn sulfides to produce disseminated sulfides. Quartz–Mn oxide oxygen isotope geothermometry constrains mineralization temperature between 18 and 118°C. Sulfur isotopes indicate the following sources of sulfide: (1) bacterial sulfate reduction within the sedimentary pile produced negative $\delta^{34}S$ values (<−20‰) in framboidal pyrite; and (2) bacterial sulfate reduction at high temperature (80–118°C) within the sedimentary pile during the infiltration of the metal-bearing brines produced Cu–Co–Zn sulfides with negative, but close to 0‰, $\delta^{34}S$ values. Isotope modeling of fluid-rock reaction and fluid mixing indicates: (1) sedimentary and marine carbonates ($\delta^{13}C$=−11.6 to −3.2‰ and $\delta^{18}O$=+19.0 to +21.8‰) precipitated from basin seawater/pore water that variably mixed with isotopically depleted meteoric waters; and (2) hydrothermal calcite ($\delta^{13}C$=−7.9 to +4.3‰ and $\delta^{18}O$=+22.1 to +25.8‰) formed by dissolution and replacement of authigenic marine calcite by downward-infiltrating metalliferous brine and brine-sediment exchange, that prior to reaction with calcite, had mixed with isotopically depleted pore water. The downward infiltration of metalliferous brine is inferred from lateral and stratigraphic metal distributions and from the concentration of Cu sulfides along the upper contact of pyrite-bearing laminae. The co-existence and textural relationships among framboidal pyrite, base metal sulfides, carbonate and Mn–Fe oxides (including magnetite) within mineralized units are consistent with carbonate replacement and high-temperature bacterial reduction within the sedimentary pile occurring simultaneously below a seawater column under predominantly oxygenated conditions.

Keywords Boléo · Stable isotopes · Copper sulfide · Manganese oxide · Strontium isotopes

Editorial handling: H. Frimmel

A. G. Conly (✉)
Department of Geology, Lakehead University,
955 Oliver Road, Thunder Bay, ON, P7B 5E1, Canada
e-mail: andrew.conly@lakeheadu.ca
Tel.: +1-807-3438463
Fax: +1-807-3467853

G. Beaudoin
Département de Géologie et de Génie Géologique,
Université Laval, Québec,
Québec, QC G1K 7P4, Canada

S. D. Scott
Marine Geology Research Laboratory, Department of Geology,
University of Toronto, 22 Russell St.,
Toronto, ON, M5S 3B1, Canada

Introduction

The Boléo district consists of multiple laterally extensive stratiform units of laminated claystone and claystone breccia that contain finely disseminated Cu–Co–Zn sulfides and oxidized sulfides. The district shares many characteristic features with other sediment-hosted strati-

form Cu deposits, including: (1) extensional rift setting; (2) lateral continuity of mineralization; (3) low-temperature, chalcocite-dominant, sulfide assemblage; (4) replacement of early diagenetic pyrite by Cu sulfides; (5) soft-sediment deformation features; (6) association with both continental red-beds and evaporite units; and (7) relationships to structural and topographic features. Consequently, previous workers have favored diagenetic, or red-bed type, models, whereby ore fluids ascended along basin faults and migrated laterally through the thick conglomerate units prior to infiltration into and reaction with reducing agents within manto strata (e.g., Touwaide 1930; Wilson and Rocha 1955; Ochoa-Landin 1998; Bailes et al. 2001).

Previous studies of the Boléo district provide few to no quantitative physicochemical constraints on the evolution of the hydrothermal system. Consequently, it is the aim of this study to better constrain the physicochemical the nature of the various fluids and the mechanism(s) involved in sulfide formation. To this effect, C/S ratios, stable (C, O and S) and radiogenic (Sr) isotopes, and Mn contents of limestone, evaporite, and conglomerate units are used to determine the nature of the water column (i.e., marine vs lacustrine, oxic vs anoxic). Stable (C, O and S) and Sr isotopes of gangue sulfate and carbonate, S isotopes of sulfide and O isotopes of Mn oxides are used to better understand the processes of mineralization and sulfate reduction, as well as the temperature of mineralization. Furthermore, modeling of C and O isotopes of calcite is used to determine the fluid mixing and fluid–rock interactions during Cu sulfide mineralization.

Geological setting

Low-grade sediment-hosted stratiform Cu–Co–Zn mineralization of the Boléo district is contained within the Santa

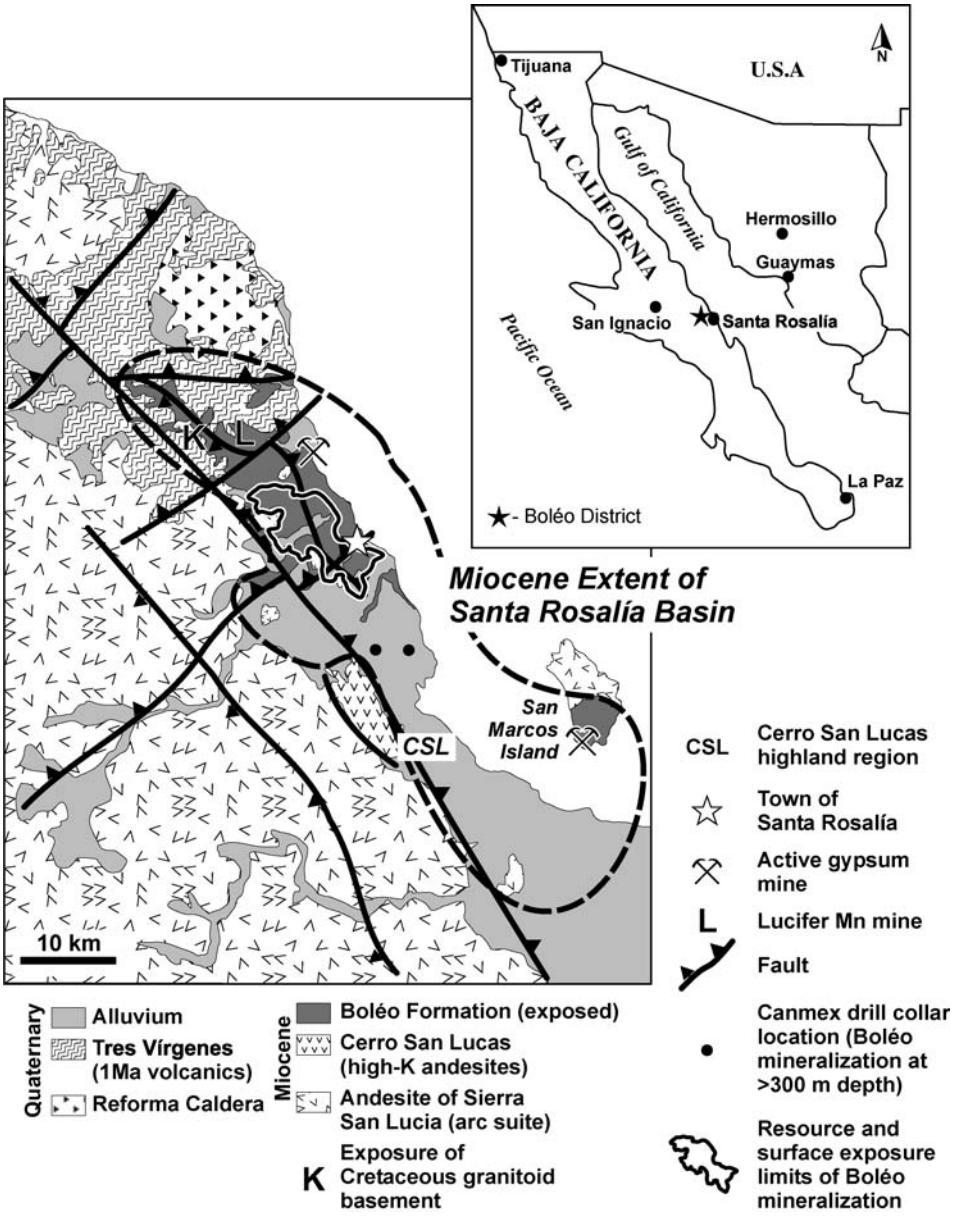

Fig. 1 Simplified geological map of the Santa Rosalía basin region and the Boléo Cu–Co–Zn district

Rosalía basin (Fig. 1), an incipient rift (Karig and Jensky 1972) basin that developed in response to Miocene continental rifting (at approximately 11 Ma; Conly et al. 2005) along the margin of the North American plate (Gastil et al. 1975). Rifting led the slow transfer of the Baja Peninsula from the North American Plate to the Pacific Plate by 5.5 to 3.6 Ma with the onset of seafloor spreading in the modern gulf (Larson 1972; Curray and Moore 1984; Lonsdale 1989). Prior to rifting, tectonic activity in the Gulf region consisted of oblique subduction of the Farallon–Guadalupe plates beneath the North American plate along the western margin of Baja California (Atwater 1989; Stock and Hodges 1989; Lonsdale 1989; Stock and Lee 1994). During this time (24–12 Ma), andesitic lavas erupted along a 500-km northwest–southeast axis forming the main peninsular escarpment (Sawlan and Smith 1984). Within the Santa Rosalía district, incipient rift volcanic rocks include 11- to 10-Ma tholeiitic basalt, 10- to 9-Ma basaltic andesite and a 9- to 8-Ma felsic tuff unit (Conly et al. 2005). High-K andesite and basaltic andesite of Cerro San Lucas (CSL) are equivalent to the post-10-Ma alkali suite along the southwestern edge of the Santa Rosalía basin (Fig. 1; Conly et al. 2005).

Marine and non-marine rift-fill sediments of the Boléo Formation are the first sedimentary deposits within the Santa Rosalía basin (Fig. 2). Basal units of the Boléo Formation include a locally distributed conglomerate (<10 m), marine limestone (<5 m), and bedded gypsum/anhydrite (<100 m), which unconformably overlies arc and syn-rift volcanic rocks. Locally, along major basin growth faults, bedded sulfates were tectonically deformed to produce brecciated mound-like diapirs (Conly 2003). Incursion of the Pacific Ocean into basins north of the Santa Rosalía basin occurred along a seaway that extended from the southern region of the Vizcaino Peninsula to north of San Ignacio and through a break in the magmatic arc and interconnected basins to the north and northeast (Fig. 1; Ledesma-Vázquez et al. 1999).

The Boléo clastic sequence consists of a series of five coarsening upward fan–delta cycles, ranging between 10 and 140 m in thickness (Wilson and Rocha 1955; Ochoa-Landin 1998; Ochoa-Landin et al. 2001). The base of each cycle consists of a tuffaceous claystone, grading upwards into siltstone, sandstone, and conglomerate. The abrupt transition from conglomerate to tuffaceous claystone marks the change from prograding fan–delta sedimentation to transgressive marine sedimentation (Bailes et al. 2001). The cyclical nature of Boléo clastic sedimentation is interpreted as the stacking of multiple prograding fan-deltas in response to basin subsidence (Conly 2003). The cyclicity is analogous to cyclothems that developed in response to episodic tectonism within extensional basins,

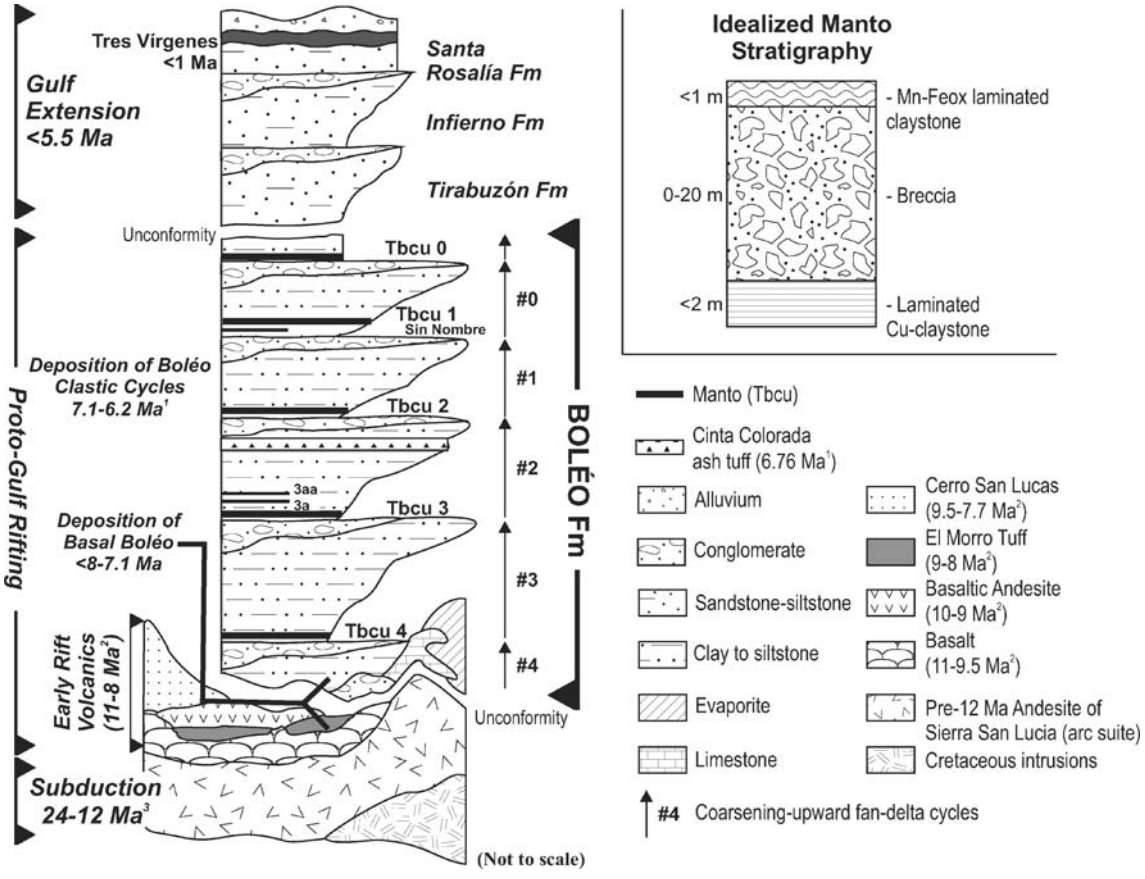

Fig. 2 Regional stratigraphic section of the Santa Rosalía basin (modified after Wilson and Rocha 1955). Inset is the generalized stratigraphy of a Boléo manto. Age determinations from: 1—Holt et al. 2000, 2—Conly et al. 2005; Conly 2003, and 3—Sawlan and Smith 1984

which develops because fine-grained marine sedimentation responds more rapidly to subsidence than fan/alluvial environments, especially if the basin is connected to open marine waters (Steel et al. 1977; Blair and Bilodeau 1988). Based on ^{40}Ar–^{39}Ar geochronology and magnetostratigraphy, Holt et al. (2000) constrained the timing of Boléo clastic sedimentation between 7.1 and 6.2 Ma.

Laterally extensive zones of conformable sulfide mineralization with pervasive supergene oxide overprint are hosted within the basal claystone of each fan–delta cycle of the Boléo clastic sequence, and primarily occur within two smaller sub-basins in the northern part of the Santa Rosalía basin (Figs. 1, 3 and 4). Mineralization extends for more than 90 km^2 with delineated reserves of 70 Mt grading 1.29% Cu, 0.09% Co, and 0.62% Zn, and a total resource of 464 Mt grading 0.70% Cu, 0.06% Co, and 0.71% Zn (Bailes et al. 2001). Mineralization is found in eight mineralized beds, or mantos, comprised of a finely laminated tuffaceous claystone base (1–2 m) overlain by polymictic claystone breccia (1–20 m), and capped by Mn–Fe oxide-rich laminated claystone (<2 m) (Fig. 5a–d). The lower claystone contains soft-sediment deformation structures (Fig. 5a,b), whereas, the upper claystone is commonly brecciated. The laminated claystone is interpreted to be deeper water facies representing periods of low sedimentation and quiescence during marine transgressive events (Bailes et al. 2001; Conly 2003). The claystone breccia is interpreted to be a tectonically triggered debris flow (Bailes et al. 2001; Conly 2003), which is consistent with the evidence for minimal lateral transport of debris fragments (where in some locations the bedform can be easily recreated due to the "jigsaw-like" fit of the breccia fragments; e.g., Pufahl and Fralick 2004). Furthermore, claystone to sandstone interbeds within the breccias are generally massive to planar-laminated, which further implies minimal lateral transport of sediment. Consequently, the breccias represent discrete depositional (slumping) events, consistent with tectonically induced subsidence and not time-transgressive prograding sedimentation. The mantos include sulfide, oxide, and mixed sulfide-oxide facies. The sulfide facies contains pyrite+chalcocite+covellite± chalcopyrite±bornite±sphalerite, with trace amounts of primary magnetite and Mn oxide (Fig. 6). Chalcocite and covellite are the most abundant sulfides within the basal laminated claystone facies and laminated breccia fragments, where they are found to replace framboidal pyrite (Fig. 6a–d). Sulfide textures within the breccia matrix are more varied and include disseminated grains, vug fillings,

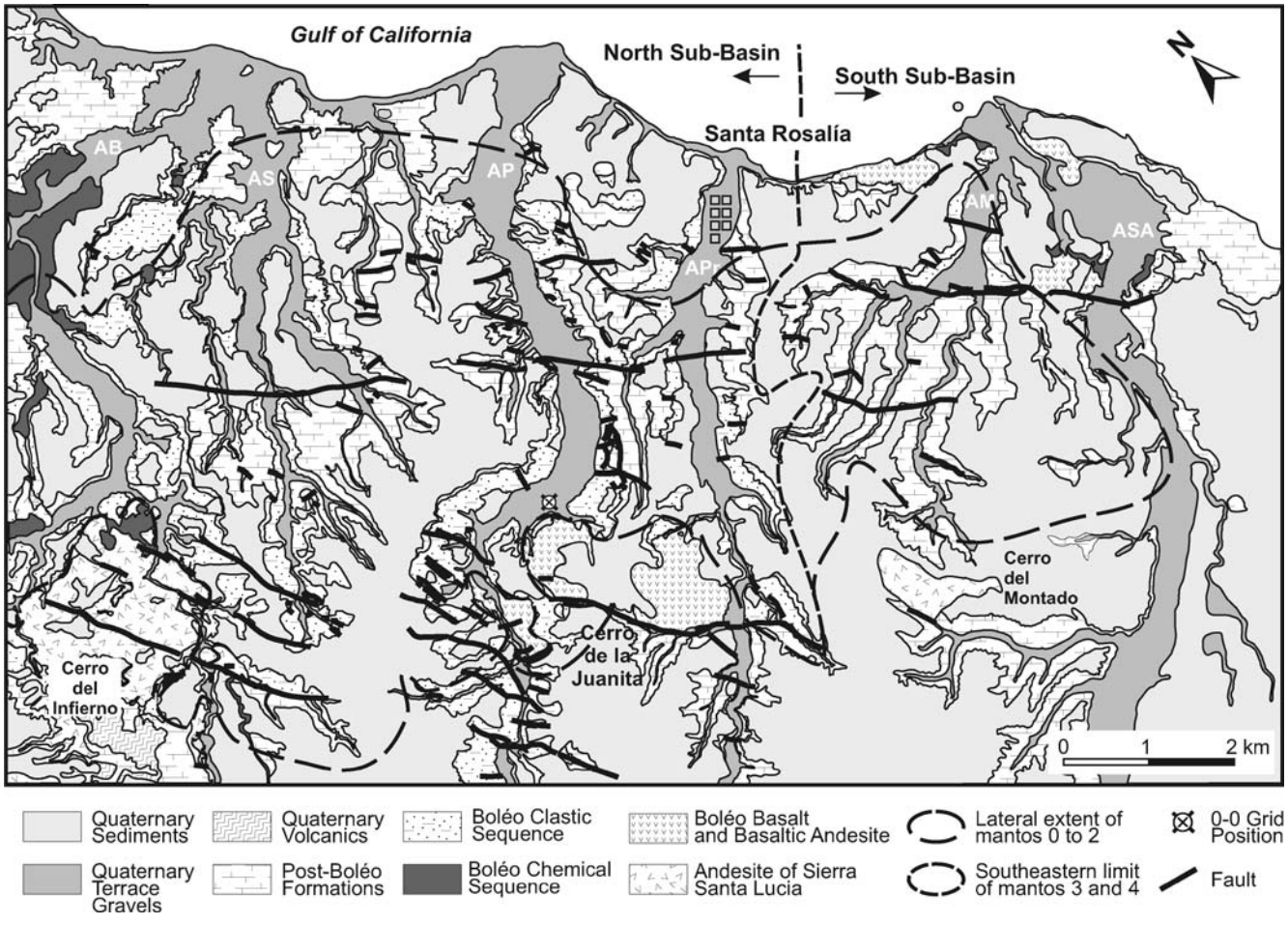

Fig. 3 Geological map of the Boléo Cu–Co–Zn district (modified from Wilson and Rocha 1955). *AB* Arroyo del Boléo, *AS* Arroyo de la Soledad, *AP* Arroyo del Purgatorio, *Apr* Arroyo de la Providencia, *AM* Arroyo del Montado, *ASA* Arroyo de Santa Agueda

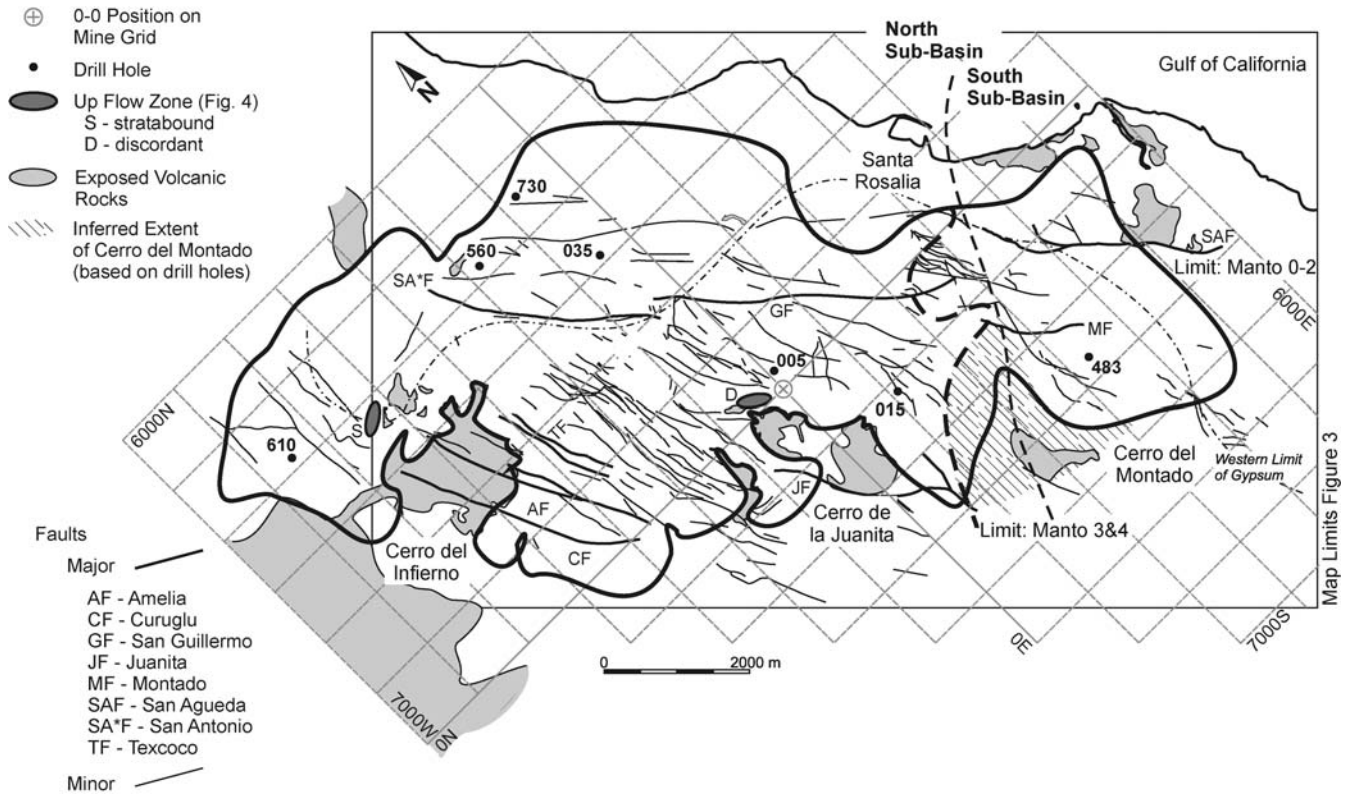

Fig. 4 Map showing the lateral resource extent of mantos 3 and 4 (north sub-basin) and mantos 0 to 2 (north and south sub-basins), and the surface trace of major and minor faults (from Wilson and Rocha 1955; unpublished maps by International Curator Resources). Grid spacing is at 1,000-m intervals. Also shown are the collar locations of drill holes used for the vertical metal profiles (Fig. 10)

precipitates along the edges of clasts, replacement of earlier formed sulfides and veins. The oxide facies is characterized by the pervasive replacement of sulfidic rock by Mn–Fe–Cu oxides due to supergene weathering. Gangue phases present in all facies include montmorillonite, gypsum, barite, Ca–Mg–Fe carbonates, chalcedony, Mn–Fe oxides, and volcanic fragments.

Sampling and analytical methods

Detailed field work was carried out throughout the Santa Rosalía basin and central Baja California region; although, emphasis was placed on sampling of manto units throughout the Boléo district. Field work for this study consisted of the re-logging of 11 drill cores, with re-logging of only the manto sections from an additional 52 drill cores, mapping of 16 trenches and extensive sampling of drill core (n=698), trenches (n=94) and outcrops (n=212).

Minerals for isotopic analyses were separated by hand-picking and gravitation methods, with adhered clays being removed by flocculation in deionized-distilled water (DIDW). The fine-grained (typically <50 μm) and intergrown nature of the sulfides and gangue minerals makes it impossible to prepare monomineralic separates. Consequently, fractionation between co-existing sulfide phases cannot be fully assessed. Sample heterogeneity was assessed by X-ray diffraction (XRD), with only the least heterogeneous samples being used for isotopic analysis. The primary concern of sample heterogeneity is the presence of pyrite (see below). Regardless of any precautionary steps taken, the isotopic data represents "averaged" or bulk-rock compositions rather than the composition of individual hydrothermal phases.

The $\delta^{34}S$ and $\delta^{18}O$ isotope ratios of manto barite and evaporitic gypsum-anhydrite were determined at the University of Waterloo by elemental analyzer-continuous flow-isotope ratio mass spectrometry (EA-CF-IRMS) (Table 1). Sulfur and oxygen isotope ratios were measured on separate aliquots. Oxygen in sulfate was liberated by EA combustion of barite (Kornexl et al. 1999), with gypsum and anhydrite being dissolved and reprecipitated as barite. The resulting fractionation effect of conversion to barite is approximately +0.02‰. Sulfur and oxygen isotope ratios are reported relative Canyon Diablo Troilite (CDT) and Standard Mean Ocean Water (SMOW), respectively. Internal laboratory standards were calibrated with international standards NBS-123 (sphalerite) and NBS-127 (barite), which yield routine precisions (1σ) of ±0.2‰ and ±0.5‰ for $\delta^{34}S$ and $\delta^{18}O$, respectively. Sulfide (±trace barite) $\delta^{34}S$ was determined by EA-CF-IRMS at Queen's University. Soluble sulfate was removed by dissolution in

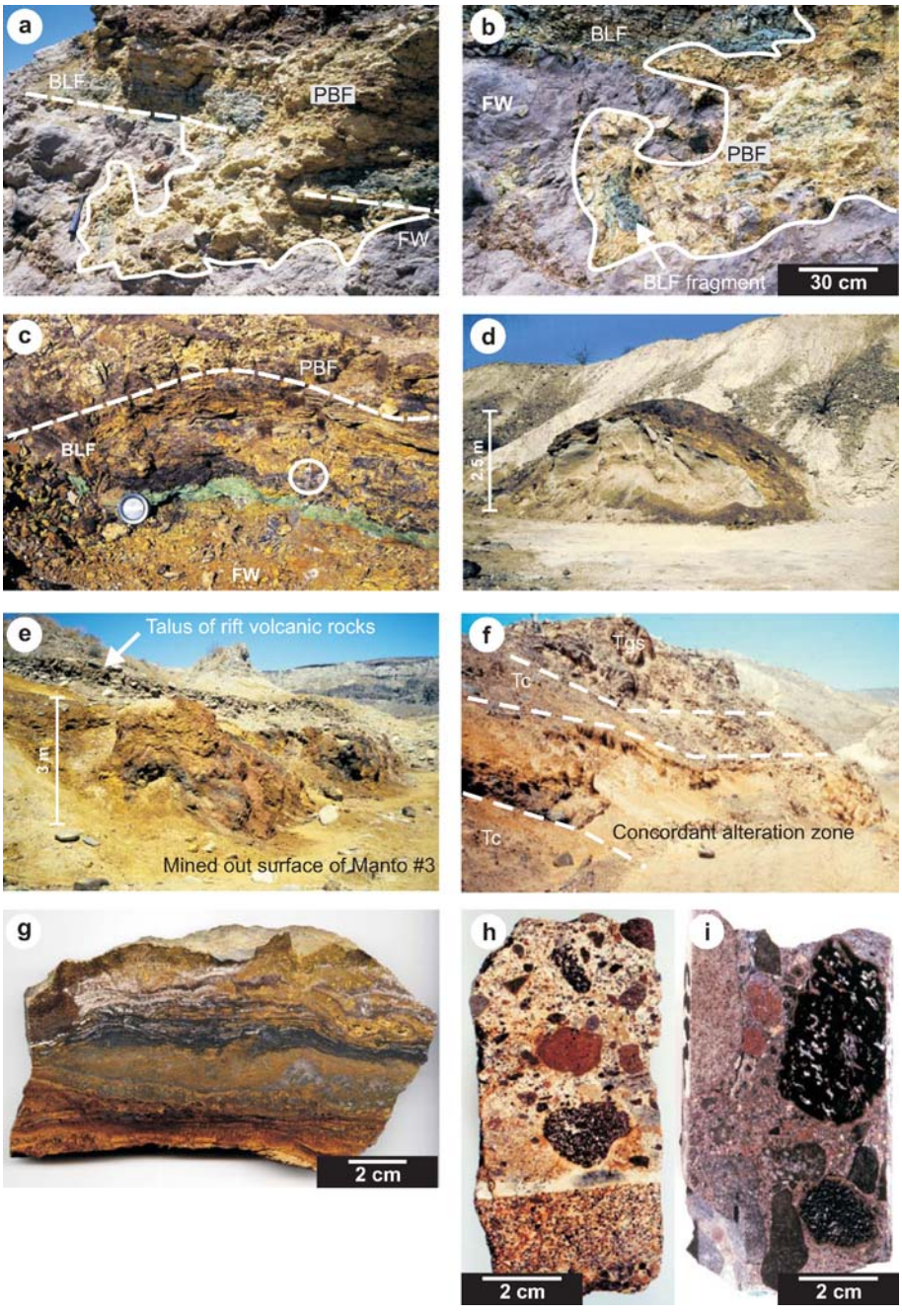

Fig. 5 **a** Soft-sediment injection of manto 3a breccia into bedded footwall claystone (breccia is outlined by *solid line*), where rip-up fragments of the basal laminated facies (*darker green* color due to Cu-oxides) have been incorporated into the breccia slump (*long dashed line* marks the footwall contact). **b** Close-up view of the Cu-rich laminated fragments entrained within the slump show in photograph "a" (*BFL* Basal laminated claystone facies, *PBF* polymictic claystone breccia facies, *FW* footwall). **c** Highly oxidized basal laminated claystone facies of manto 2 with pervasive Fe oxide (*yellow-orange*) and Mn oxide (*black*) alteration, patchy Si alteration (*circle*) and malachite alteration of sulfide-rich laminae. **d** Upper laminated facies in the oxide zone with pervasive Fe–Mn oxide alteration (folded bedding in response to deformation resulting from compaction loading and tectonic activity related to the modern Gulf of California). **e** Discordant Mn–Fe–Si alteration zone along the contact between manto 3 and the underlying arc to rift volcanic rocks (Tc) and Tirabuzón (Gloria) Formation fossiliferous sandstone (Tgs). **f** Concordant Mn–Fe–Si alteration (lateral extent of photograph is ~50 m) at the contact between Boléo Formation clastic units (altered zone) and arc and rift volcanic rocks (*Tc*) (*Tgs*Gloria formation fossiliferous sandstone). **g** Mn–Fe–Si alteration concordant with bedding. Pervasive Si alteration overprints earlier Mn oxide (*black*), Fe oxide (*red to orange*) and carbonate+smectite+sulfate (*chalky white*) alteration. **h** Drill-core photograph of clay-altered conglomerate. **i** Drill-core photograph of least-altered conglomerate

40°C DIDW, and $\delta^{34}S$ ratios were measured on the produced SO_2. Results are reported relative to CDT, with a precision (1σ) for NBS-123 (sphalerite) and NBS-128 (barite) of ±0.2‰ and ±0.5‰, respectively. Sulfur and carbon contents of sulfide-bearing manto rock and Boléo clastic sedimentary rocks were determined by Leco infrared analysis. Sulfide-sulfate species of sulfide separates were determined on powders using the $S-K_{\beta 1x}/S-K_{\alpha 1}$ peak ratio on XRF spectra (Conly 2003). Species differentiation is possible for samples with >75 wt% sulfide sulfur, where the sulfide-sulfate contents can be estimated with an accuracy of ±5 wt% (Table 2).

Mixed carbonates (calcite–dolomite–siderite) were analyzed for $\delta^{13}C$ and $\delta^{18}O$ at the University of Ottawa. Carbon dioxide was sequentially extracted using phosphoric acid (McCrea 1950) from: (1) calcite after 4 h at 25°C; (2) dolomite at after 48 h at 50°C; and (3) siderite after 4 days at 50°C. All $\delta^{18}O$ and $\delta^{13}C$ values are reported relative to SMOW and PDB (Pee Dee Belemnite), respectively. The routine precision (1σ) on a pure carbonate analysis for both ^{18}O and ^{13}C is ±0.1‰, based on NBS-18, 19 and IAEA-CO-8, 9. Isotopic compositions derived from calcite–siderite sequential extraction are reproducible within 0.4‰, and generally 0.1‰, based on one duplicate

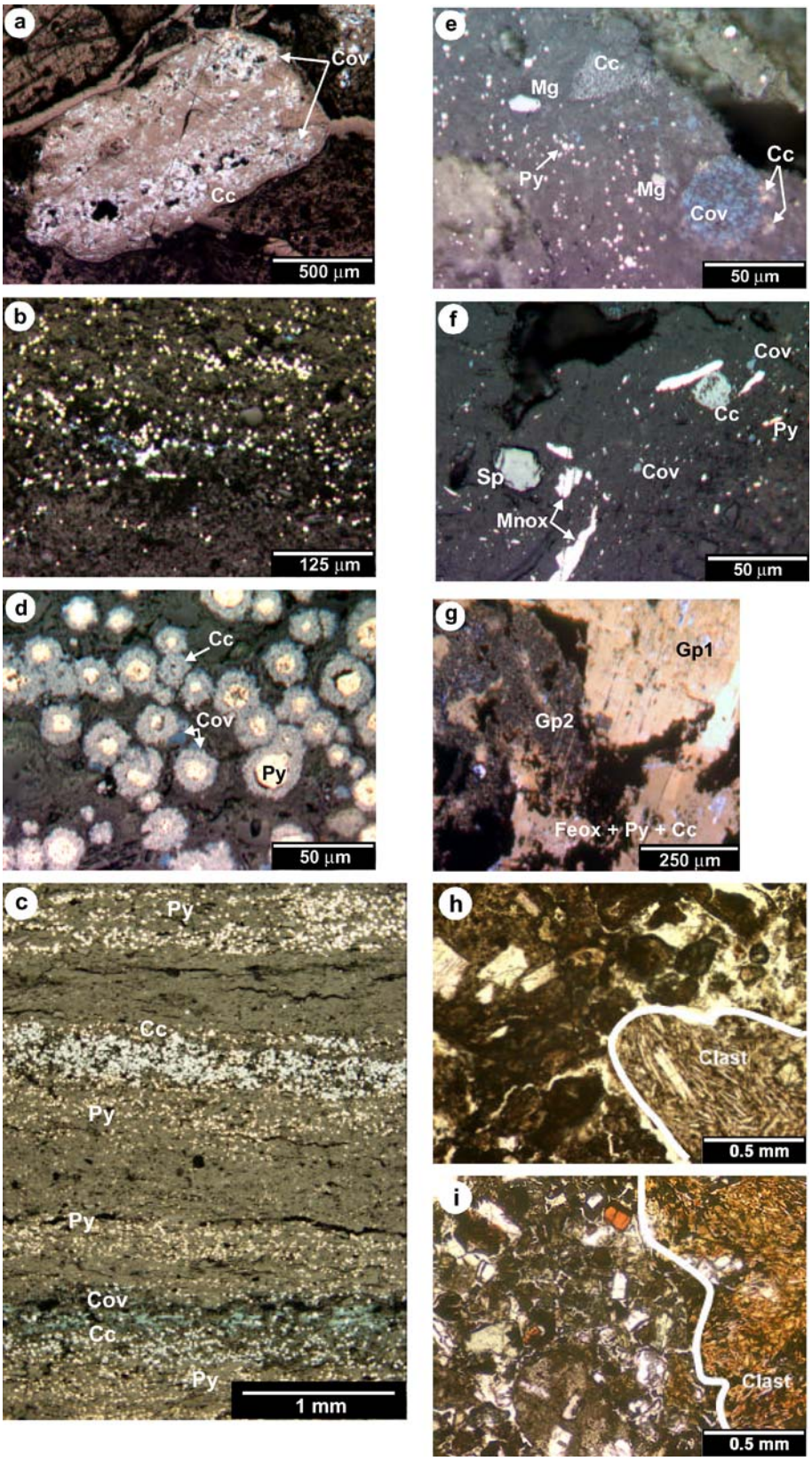

Fig. 6 Reflected light (unless otherwise stated) photomicrographs of Boléo sulfide and primary oxide mineralization: **a** laminated claystone rip-up fragment with chalcocite and covellite replacement of pyrite (not distinguishable) contained within the fragment; **b** finely disseminated framboidal pyrite (along bedding plans of laminated claystone; **c** chalcocite± covellite replacement of framboidal pyrite restricted to the upper part of pyritic laminations within planar laminated claystone; **d** framboidal pyrite replaced by chalcocite and covellite; **e** disseminated magnetite associated with finely disseminated pyrite (*bright grains*), whereas, covellite and chalcocite occur both as fine disseminations in the matrix as well as replacing sulfides in clasts; **f** equant sphalerite grain with disseminated manganese oxide, pyrite, chalcocite and covellite; **g** dissolution of primary coarse-grained gypsum (*Gp1*) with infilling by fine-grained gypsum (*Gp2*) and Fe oxides, pyrite and chalcocite (*Feox+Py+Cc*, *black aggregates*) (cross-polarized transmitted light); **h** photomicrograph (plane polarized light) of altered conglomerate, which consists of pervasively hematized andesite clasts and a higher abundance of Fe oxide grain aggregates within the matrix. Only large euhedral crystals of plagioclase remain. Other matrix constituents include smectite (montmorillonite), carbonate, gypsum and barite; **i**) photomicrograph (plane polarized light) of least-altered conglomerate, which consists of weakly hematized andesite clasts in a detrital-rich matrix composed of plagioclase (*bright laths*), titanomagnetite (*dark equant grains*) and silty-clay sized detritus (*mottled texture*). Fe-oxidation of matrix is minor. Minerals: *Cc* Chalcocite, *Ccp* chalcopyrite, *Cov* covellite, *Mg* magnetite, *Mnox* manganese oxide, *Sp* sphalerite, *Gp* gypsum, *Feox* undifferentiated hematite+ goethite

(429–50.70; Table 3). Mixed calcite–dolomite samples do not have the reproducibility of pure carbonate or calcite–siderite, with $\delta^{18}O$ and $\delta^{13}C$ values of the calcite of the duplicate (96-0827-040; Table 3) differing by 0.7‰ and 0.6‰. The lower precision may be attributed to (1) sample heterogeneity or (2) grain size less than the optimal range

Table 1 Oxygen, sulfur and strontium isotope compositions of Boléo sulfate

Sample	Phase	Unit	$\delta^{18}O$ (‰)	$\delta^{34}S$ (‰)	$^{87}Sr/^{86}Sr$
Basal gypsum (Tbg) sequence					
454-36.85	Gp	Bed	6.5	21.7	0.70715
Repeat			6.5	22.0	
746-108.54	Anh	Bed	13.1	22.3	0.70852
CPP6-188.54	Anh	Bed	12.8	22.1	0.70802
96-0827-026	Gp	Mound	10.8	22.6	
Repeat				23.5	
96-0924-136	Gp>Anh	Bed	6.9	21.6	
00-0503-217	Gp	Mound	8.4	21.6	0.70754
00-0503-218	Gp>Anh	Mound	8.7	21.9	
00-0503-220	Gp>Anh	Mound	8.8	21.7	
Repeat				21.8	
Manto sulfate					
96-TR072-1.50	Brt	pobx#3	10.7	18.9	0.70580
Repeat			10.9		
397-198.90	Brt	pobx#3	11.2	17.5	0.70602
Repeat			11.3	17.2	
429-48.65	Brt	pobx#4	14.5	−5.1	0.70716
Repeat			15.0		
527-83.25	Cls	pobx#3	12.3	21.1	0.70684
Repeat			21.1		

$\delta^{18}O$ is reported relative to SMOW, and $\delta^{34}S$ is reported relative to CDT

Mineralogy determined by XRD

Gp Gypsum, *Anh* anhydrite, *Brt* barite, *Cls* celestite, *Bed* laminated or bedded sample, *Mound* brecciated fragments from diapir (mound) structures, *pobx#* disseminated grains of polymitic claystone breccia of corresponding manto #

of 0.125 to 0.25 mm, which may have resulted in the partial extraction of dolomite with calcite. The extent of post-depositional alteration was assessed using whole-rock Mn contents of basal Boléo and Tirabuzón limestone (Veizer and Fritz 1976), which were measured by XRF. Mn concentrations are reported on a Si–Al–Ti-free basis to remove chemical inputs from detrital silicates. Sample volumes of manto carbonates were insufficient for XRF analysis. Least-altered samples have Mn values of ~1 wt%, based on the Mn concentration for Tirabuzón Formation coquina (Table 3).

Oxygen isotope analyses of Mn oxide and silicate were performed at the Université Laval, with a subset of replicate and silicate residues analyzed at Queen's University (Table 4). Oxygen was extracted using bromine pentafluoride (BrF_5) and converted to CO_2 following the methods of Clayton and Mayeda (1963). Silicate separates were prepared by $HCl–HNO_3–H_2O_2$ digestion of Mn oxide. All isotope ratios are reported relative to SMOW. Reproducibility of values based on replicate analyses of NSB-28 (quartz) and an internal Laval standard is ±0.2‰ (1σ).

The $^{87}Sr/^{86}Sr$ isotopic composition of Boléo carbonate, sulfate, silicate and manganese oxide samples were determined at Carleton University using standard cation exchange techniques, followed by thermal ionization mass spectrometry (Cousens 1996). Samples were dissolved in three steps using 12 N HNO_3, 8 N HNO_3, and finally 6 N HCl. Silicate samples were initially treated with 50% HF. The samples were dried and redissolved in 2.5 N HCl for Sr separation. Isotope ratios were normalized to $^{86}Sr/^{88}Sr=0.11940$. The average $^{87}Sr/^{86}Sr$ value obtained for NIST SRM987 was 0.710265±7 (n=3), within 2σ uncertainty of the laboratory value (0.710257±22, n=13).

Analytical results

Bedded anhydrite from the basal gypsum sequence has typical marine $\delta^{18}O$ (+12.8 to +13.1‰) and $\delta^{34}S$ (+22.1 to +22.3‰) values, with strontium isotope ratios being less radiogenic (0.70850–0.70802) than 8 to 6 Ma Miocene seawater (0.70893 to 0.70899; Howarth and McArthur 1997). Other Boléo sulfates yield two groups (Fig. 7): (1) bedded anhydrite–mound/bedded gypsum, which display a greater variance in $\delta^{18}O$ (+6.5 to +10.8‰) and a narrow range in $\delta^{34}S$ (+21.6 to +23.5‰) and $^{87}Sr/^{86}Sr$ (0.70715–0.70754), and (2) bedded anhydrite–manto barite, which display a small variation in $\delta^{18}O$ (+10.7 to +12.3‰) and significant differences in $\delta^{34}S$ (+17.2 to +21.1‰) and $^{87}Sr/^{86}Sr$ (0.70580–0.70684). The barite sample with a low $\delta^{34}S$ value (−5.1‰), similar to negative $\delta^{34}S$ values for manto sulfide (Table 2), is interpreted to be a product of oxidation of manto sulfide (e.g., Ohmoto and Rye 1979). All Boléo sulfates have $^{87}Sr/^{86}Sr$ values that plot between normal marine values and the range for basement plutonic and volcanic rocks (0.70372–0.70447; Fig. 7b).

Boléo calcite from mantos, basal limestone, and intraformational conglomerate cement define an array of decreasing $\delta^{13}C$ and $\delta^{18}O$, with values from −9.7 to −2.4‰ and 18.6 to 21.5‰, respectively, between values for normal marine and fresh water calcite (Fig. 7c). Manto calcite is, generally, enriched in both heavy carbon and oxygen ($\delta^{13}C>2‰$ and $\delta^{18}O>21‰$), compared to both types of sedimentary calcite. Exceptions include: (1) two manto calcite samples with $\delta^{13}C$ and $\delta^{18}O$ values less than 2‰ and 21‰, respectively, which are isotopically similar to sedimentary calcite; and (2) two high Mn (>2 wt%) calcite analyses from the basal limestone sequence, which are similar to isotopically heavy manto calcite and normal marine calcite (Fig. 7c). $^{87}Sr/^{86}Sr_{bulk\ carbonate}$ ratios are similar for the three types of carbonate (Fig. 7d), but $\delta^{18}O_{calcite}$ define two groups (Fig. 7d): Group I) manto calcite and Mn-rich basal limestone, which display a narrow range in $\delta^{18}O$; and Group II) basal limestone, sedimentary cement, and low $\delta^{18}O$ manto calcite that form an array between normal marine calcite and basement volcanic and plutonic rocks. Small amounts of siderite and dolomite occurring in manto and basal limestone units are in isotopic disequilibrium with co-existing calcite (Fig. 8).

Bulk-rock (oxide+silicate) $\delta^{18}O$ values for Mn oxide range between 0 and +20.8‰. Quartz and albite, on average, constitute around 20%, and up to 65.4%, of the

Table 2 Carbon, sulfur and sulfur isotope compositions for Boléo mantos and sedimentary rocks

Sample	Bulk rock							Sulfide separates				
	C^T	C^{CO2}	TOC	S^{Bulk}	S	SO_4^{2-}	S^{Bulk}/TOC	$\delta^{34}S$	S^{Sep}	$BaSO_4$	SO_4	S_S
Mantos	%	%	%	%	%	%		‰	%	%	%	%
272-180.40	0.06	b.d.	0.07	0.84	0.51	0.33	12.00	−6.1	6.30	0.11	0.33	5.86
272-181.25	0.37	b.d.	0.39	3.37	1.67	1.70	8.64	−3.7	20.96	0.29	7.73	12.94
281-145.04	0.11	b.d.	0.12	2.24	1.72	0.52	18.67	−3.8 (−4.1)	6.65	b.d.	0.68	5.97
345-42.50	2.02	0.90	1.12	3.16	2.79	0.37	2.82	n.d.	n.d.	n.d.	n.d.	n.d.
370-58.00	0.35	0.02	0.33	4.60	3.93	0.67	13.94	−5.6	2.53	0.25	0.65	1.63
370-58.00c	n.d.	n.d.	n.d.	n.d.	n.d.	n.d.	n.d.	−1.8	7.11	0.70	0.44	5.97
391-160.30	0.07	0.03	0.04	1.19	0.90	0.29	29.75	−8	5.63	0.05	0.39	5.19
391-161.45	n.d.	n.d.	n.d.	n.d.	n.d.	n.d.	n.d.	−5.4 (−5.3)	6.20	0.02	b.s.	6.18
466-94.80	0.05	<0.01	0.05	1.97	0.95	1.02	39.40	−7.6	6.59	b.d.	2.58	4.01
466-95.50	0.67	0.28	0.39	3.22	1.54	1.68	8.26	−9.6	8.96	b.d.	2.47	6.49
527-74.28	5.29	4.08	1.21	4.69	4.69	b.d.	3.88	−10.7	2.20	0.01	0.38	1.81
527-75.60	0.56	0.41	0.15	4.43	4.43	b.d.	29.53	−4.5	6.63	0.10	0.37	6.16
527-75.70	0.78	0.64	0.14	1.39	0.99	0.40	9.93	−3.3 (−3.0)	5.79	0.08	0.13	5.58
527-79.20	3.63	2.44	1.19	2.46	2.00	0.46	2.07	−13.7	1.99	b.d.	1.22	0.77
Claystones and siltstones												
391-159.20	0.06	b.d.	0.06	0.25	0.13	0.12	4.17					
455-140.00	0.16	0.15	0.01	<0.01	b.d.	<0.01	0.50					
484-196.70	0.05	0.04	0.01	0.01	b.d.	0.01	1.30					
724-41.25	0.08	0.07	0.01	0.01	b.d.	0.01	1.10					
Conglomerates (matrix only)												
96-0906-070M	0.06	0.04	0.02	<0.01	<0.01	<0.01	0.25					
391-168.4M	0.18	0.15	0.03	<0.01	<0.01	<0.01	0.17					
484-173.42M	0.10	0.08	0.02	0.06	0.04	0.02	3.00					
560-40.0M	0.08	0.05	0.03	0.03	<0.01	0.03	1.00					
705-101.0M	3.98	3.92	0.06	0.03	<0.01	0.03	0.50					
96-TR068-0.0M	0.04	0.02	0.02	0.05	<0.01	0.05	2.50					

Bulk rock: C and S determined on whole-rock samples by LECO infrared at the University of Toronto. S/C ratios for samples with b.d. values are determined using concentrations equal to one-half the minimum detection limit of 0.01
C^T Total carbon, C^{CO2} carbonate, *TOC* total organic carbon, S^{Bulk} total sulfur of whole rock sample, *S* sulfide+insoluble sulfate (barite), SO_4^{2-} water soluble sulfate (gypsum+anhydrite), *bd* below detection limit, *nd* not determined
Sulfide separate: $\delta^{34}S$ measured by EA-CF-IRMS at Queen's University and is relative to CDT. Replicate analyses in brackets. S^{Sep} equals total sulfur, as determined by XRF for sulfide separate, which was hand- and gravimetrically separated from the bulk sample. XRF analyses were performed at the University of Toronto. $BaSO_4$ corresponds to sulfur as barite and determined by XRF, assuming all Ba occurs as barite. SO_4 (soluble sulfate sulfur) and S_S (sulfide sulfur) determined by XRF $SK_{\beta 1x}/SK_{\alpha 1}$-peak-ratio method (see Conly 2003). Sample 370-58.00c corresponds to a sulfide-rich portion of the breccia matrix that was hand-separated

bulk samples and have $\delta^{18}O$ values ranging from +13.2 to +26.1‰. Manganese oxide compositions calculated after removing the isotopic composition of silicate inclusions, using the mass balance relationships of Bar-Matthews and Matthews (1990), yield $\delta^{18}O$ values between −0.2 and +12.5‰. Replicate analyses for two Mn oxide–quartz vein pairs yielded consistent isotopic compositions. $^{87}Sr/^{86}Sr$ ratios for bulk samples are between 0.70606 and 0.70750, within the range observed for manto carbonates and sulfates, and have no correlation with calculated $\delta^{18}O$ (Conly 2003).

Fine-grained clastic units and conglomerates are characterized by low total organic carbon (TOC) and total sulfur bulk-rock contents, with highly variable S/C ratios that range from 0.17 to 4.17 (Table 2). Fine-grained clay and silt units at the base of the fan–delta system have S/C >2 due to the high abundance of framboidal pyrite. S/C ratios between 0.36 and 2 for claystone/siltstone and conglomerate units are not caused by increased sulfide content because these samples are also characterized by low sulfide sulfur contents (<0.01 wt%) and slightly elevated sulfate sulfur contents (0.01 to 0.05 wt%) for the bulk rock. The S/C ratio of manto units is highly variable and ranges between 2.07 and 39.40.

The sulfur isotope ratios of Cu (±Co, Zn)-rich sulfide range from −13.7 to −1.8‰ (Fig. 9 and Table 2), and are lower than for pyrite-rich samples ($\delta^{34}S$=−33.6 to −10.9‰; Ochoa-Landin 1998). Because sulfides and sulfates co-exist, it is necessary to determine if the higher $\delta^{34}S$ values reflect contamination by heavy insoluble sulfate. XRF $Sk_{\beta 1x}/SK_{\alpha}$ peak ratio determinations of sulfur in sulfide separates show that sulfur occurring as sulfide generally accounts for >60% of the total sulfur (Table 2). With the exception of the two magnetite-rich samples (527-74.28 and 79.20), sulfide concentrates consist predominantly of

chalcocite followed by covellite and bornite/chalcopyrite, with 41.64 to 63.46 wt% Cu (Conly 2003), and smaller but variable amounts of silicate material. Pyrite, sphalerite, and galena have low-to-trace abundances based on concentrations of Fe_2O_3 (<6 wt%) and Zn+Pb (<1.5 wt% combined; Conly 2003). Prior to isotopic analysis, soluble sulfate was removed from sulfide separates using 40°C DIDW, in which barite (±celestite) is insoluble. Contamination by barite, however, is minimal with less than 0.7 wt% $BaSO_4$ in sulfide concentrates (Conly 2003). Mass balance indicates that more than 2% sulfur sulfate, using barite with a $\delta^{34}S$ value of +19.2‰ (average for manto sulfate; Table 1), is required to exceed the ±0.5‰ analytical uncertainty. The different sulfur isotope composition for these two concentrates likely reflects higher pyrite abundance, indicated by a higher Fe content (1.64 vs. 0.43 wt% Fe; Conly 2003), for the concentrate with lower $\delta^{34}S$. The difference in $\delta^{34}S$ values between this study and Ochoa-Landin (1998) is not due to isotopic contamination by barite but rather, to differences in pyrite content. However, a poor correlation between Fe and $\delta^{34}S$ (r^2= −0.42) for samples from this study indicates that pyrite alone cannot account for the isotope composition differences, which must, therefore, also reflect differences in the source(s) of reduced sulfur.

Table 3 Oxygen, sulfur, and strontium isotope compositions of Boléo carbonate

Sample	Phase	Unit	$\delta^{18}O$ (‰)	$\delta^{13}C$ (‰)	$^{87}Sr/^{86}Sr$	MnO (%)
Basal and tirabuzón limestone						
96-0810-011	Cal	Tbl	20.8	−6.0	0.70688	1.51
96-0827-040	Dol	Tbl^{strm}	28.7	4.3	0.70682	2.98
	Repeat		28.3	4.0		
	Cal		24.6	0.0		
	Repeat		25.3	0.6		
96-0910-099	Dol	Tbl^{fsl}	29.3	4.4	0.70700	4.39
	Cal		26.2	−0.6		
96-0921-126	Cal	Tgl^{fsl}	19.5	−7.7	0.70648	0.93
97-0228-169	Cal	St-alt	22.1	−3.8		
Conglomerate						
036-82.00	Cal	Tbc#3	18.7	−9.7	0.70689	
429-53.70	Cal	Tbc#4	18.6	−9.6		
705-101.00	Dol	Tbc#3	24.4	−4.4	0.70697	
97-0220-140	Cal	Tc-bx	20.4	−2.4	0.70574	
Manto carbonate						
032-21.16	Dol	pobx#2	23.9	−6.6		
294-122.00	Cal		25.8	4.3	0.70765	
294-222.20	Sd	pobx#2	24.7	−8.5		
345-42.50a	Sd	lam#3	25.1	−6.2	0.70673	
	Cal		19.0	−11.6		
345-42.50b	Sd	lam#3	23.4	−6.8		
397-198.90a	Cal		24.2	−1.9		
	Sd		24.3	−2.7		
397-198.90b	Cal	pobx#3	24.7	−1.4		
397-202.11	Sd	pobx#3	24.5	−2.9	0.70644	
	Cal		23.9	−2.6		
397-204.24	Cal		24.5	−4.7		
	Sd		23.9	−4.9		
429-50.70	Cal	pobx#4	21.5	−3.1	0.70697	
	Repeat		21.8	−3.2		
	Sd		24.4	0.0		
	Repeat		24.3	−0.4		
429-52.95	Cal	pobx#4	23.6	−3.8		
451-86.04	Cal	lam#1	25.0	−1.3		
455-90.97	Cal	pobx#0	25.6	1.4	0.70747	
	Repeat		25.6	1.5		
520-112.25	Cal	lam#0	22.5	−6.1		
527-74.28	Sd	pobx#3	26.1	−9.2		
	Cal		22.1	−7.9		
671-102.20	Sd		25.6	−9.1		
709-52.15	Cal	pobx#3	23.2	−7.7		

$\delta^{18}O$ is reported relative to SMOW and $\delta^{13}C$ is reported relative to PDB. O and C isotope data were corrected for fractionation using the carbonate–phosphoric acid factors of 1.01025 for calcite (Friedman and O'Neil 1977; Sharma and Clayton 1965), 1.01065 for dolomite and 1.010454 for siderite (Rosenbaum and Sheppard 1986). Sr compositions are of bulk carbonate. Mn concentrations determined by XRF on press powder pellets, with concentrations reported on an Si–Al-free basis to remove detrital quartz
Mineralogy determined by XRD
Cal Calcite, *Dol* dolomite, *Sd* siderite, *Tbl* Boléo limestone, *Tgl* Tirabuzon limestone, *strm* stromatolitic, *fsl* fossiliferous, *St-alt* strata-bound alteration zone, *Tbc#* Boléo conglomerate, *Tc-bx* carbonate cement of brecciated arc-to-rift volcanic rocks, *pobx#* polymitic breccia facies of Boléo manto, *lam#* basal laminated facies of Boléo manto

Discussion

Hydrothermal fluid flow

In the absence of direct fluid data, understanding the evolution of the mineralizing fluid can only be deduced from mineralogical, geochemical, and isotopic compositions of mineralized and associated rocks. However, to interpret such data, it is necessary to determine the flow pathway(s) of the mineralizing fluids. An understanding of the nature of hydrothermal fluid flow within the district is required to better constrain the nature and role of end-member fluids (e.g., pore water, seawater, formation waters, vent fluids), fluid mixing, and fluid-rock interactions involved in sulfide genesis.

Existing flow models for Boléo presume that the hydrothermal fluids initially ascended along basin faults and then laterally along either permeable clastic units immediately below the manto or the breccia facies (Wilson and Rocha 1955; Bailes et al. 2001). It is unclear whether the migration of fluids from the underlying clastic units is

due to upward vertical diffusion through the overlying manto sediments (Wilson and Rocha 1955) or along subvertical conduits in poorly consolidated Boléo sediments (Bailes et al. 2001). While we do not dispute the likelihood that fluids originated at depth and ascended along basin faults, lateral flow through permeable units and upward vertical diffusion of hydrothermal fluids is refuted on the basis of inconsistencies with regard to metal distributions, tectonic relationships, mineral textures, and geochemical and Pb isotopic composition of conglomerate units, as explained below.

The up-flow and discharge of hydrothermal fluids along basin faults is inferred from the juxtaposition of high-grade Cu±Co zones (Fig. 10) and localized discordant to strata-bound zones of pervasive Mn–Fe–Si alteration (Figs. 4 and 5e–g) to basin faults. A relationship between hydrothermal and tectonic events is further supported by: (1) the cyclical nature of the Boléo Formation clastic sequence (see above), and (2) similarities in the Cu/Zn and Co/Zn ratios of manto 1 within the south sub-basin and manto 3 in the north sub-basin (Fig. 10), which are interpreted to represent the southward migration of the locus of hydrothermal activity

Table 4 Oxygen and strontium isotope compositions of Boléo manganese oxides and silicates

Sample	Unit	Phase (Residue in Mn oxide)	Silicate %	$\delta^{18}O^{Bulk}$ (‰)	$\delta^{18}O^{Si}$ (‰)	$\delta^{18}O^{Mnox}$ (‰)	±2σ	$^{87}Sr/^{86}Sr$	T°C	±2*s*
Manto Mn oxides										
108-54.60	pobx#3	Ab	6.6	7.1	19.9	6.1	0.2			
143-8.10	lam#1	Qtz (tr Ab)	6.9	7.1	21.1	5.8	0.2			
249-47.95	pobx#2	Qtz (tr Ab)	7.3	9.1	21.1	8.1	0.3			
249-49.60	vn-pobx#2	Qtz	22.0	8.8	23.0	1.2	0.1	0.70750	52	3
			22.0	8.8	22.4	1.9	0.2		66	4
			24.6	9.4	23.3	1.6	0.1		53	3
			19.1	7.1	22.3	1.1	0.1		58	3
290-119.00	pobx#2	Qtz	7.3	0.0	22.6	−2.9	0.1	0.70685	18	2
403-114.00	lam#1	Qtz (tr Ab)	4.8	4.9	20.5	4.2	0.2			
441-118.00	lam#3a	Ab (tr Qtz)	16.2	9.7	19.0	6.6	0.3			
468-32.15	pobx#1	Ab (tr Qtz)	16.1	13.4	17.5	12.5	0.4			
520-114.00	pobx#1	Ab	3.9	1.0	19.7	−0.2	0.1	0.70606	73	3
594-63.16	pobx#4	Ab (tr Qtz)	9.7	8.7	21.1	7.3	0.3			
628-92.35	pobx#3	Ab (tr Qtz)	22.9	12.2	18.5	9.3	0.4			
671-45.45	lam#2	Ab	4.0	4.7	22.6	3.6	0.1		84	4
706-22.00	pobx#3	Ab (tr Qtz)	36.4	10.9	13.2	9.5	0.4			
743-60.20	vn-pobx#3	Qtz	45.2	18.2	24.8	7.1	0.7		102	12
			45.2	18.2	24.4	7.7	0.7		118	14
			65.4	20.1	24.3	7.3	0.9		114	18
			59.1	20.8	26.1	7.6	0.9		92	15
96-0812-023	nod#3a	Qtz (tr Ab)	4.8	5.5	16.4	5.0	0.2	0.70697		
96-TR064-5.25	nod#3a	Qtz	4.4	6.7	19.5	5.9	0.2			
Discordant to strata-bound Mn–Fe–Si alteration										
00-0502-211	St-alt	Chert		23.7						
96-0919-112	St-alt	Chert		24.9						
97-0228-168	St-alt	Jasp		24.8						
	St-alt	Qtz		31.3				0.70671		
97-0228-173	St-alt	Jasp		26.8				0.70646		
Manto silicates										
070-101.75	pobx#2	Chert		24.9						
249-49.60	pobx#2	Qtz		24.0						
294-122.00	pobx#1	Mnt		25.3				0.70695		
370-58.00	pobx#3	Mnt		21.3						
397-204.24	pobx#3	Mnt		23.1						
520-112.25	inter#1	Mnt		24.6				0.70517		
671-102.20	pobx#3aa	Mnt		18.4				0.70583		
743-59.25	pobx#3	Mnt		18.7						
		Chert		23.2						
743-60.20	pobx#3	Qtz		26.4				0.70565		

Table 4 (continued)

Sample	Unit	Phase (Residue in Mn oxide)	Silicate %	$\delta^{18}O^{Bulk}$ (‰)	$\delta^{18}O^{Si}$ (‰)	$\delta^{18}O^{Mnox}$ (‰)	±2σ	$^{87}Sr/^{86}Sr$	T°C	±2*s*
Volcanic rocks										
96-0921-125	qtz monz	w/r						0.70441		
96-0914-115	ASL	w/r						0.70399		
96-0919-123	ASL	w/r						0.70447		
96-0827-042	ASL	w/r						0.70406		
97-0306-196	CSL-Hbl	w/r						0.70403		
97-0306-190	CSL-Cpx	w/r						0.70372		

Mineralogy of analyzed phases and residual phase (after HCI–HNO_3 digestion) determined by XRD. $\delta^{18}O$ values for Mn oxide and silicates are reported relative to SMOW. $\delta^{18}O$ of Mn oxides calculated using the mass balance equations of Bar-Matthews and Matthews (1990). Errors for calculated Mn oxide $\delta^{18}O$ and temperature values following method described in Conly (2003). Temperatures calculated using the quartz-geothermometer of Zheng (1991) for only samples where co-precipitation of quartz and Mn oxide is established. Residual mineralogy (after acid digestion) of Mn oxide report, while mineralogy for Mn–Fe–Si alteration, manto silicates, and volcanic rocks corresponds to phases analyzed for isotopic determinations

Ab Albite, *Qtz* quartz, *Mnt* montmorillonite, *Chert* Mn–Fe-free microcrystalline quartz, *Jasp* jasparite/Fe (±Mn)-bearing chert, *w/r* whole rock, *tr* trace, *pobx#* polymitic claystone breccia facies of manto, *vn-pobx#* vein in breccia facies of manto, *lam#* laminated claystone facies of manto, *inter#* unmineralized interval within a manto, *qtz monz* quartz monzonite basement rock, *ASL* andesite of Sierra San Lucia (=24–12 Ma arc andesite), *CSL* Cerro San Lucas rift andesite, *Hbl* hornblende phenocrysts, *Cpx* clinopyroxene phenocrysts, *St-alt* strata-bound alteration zone

in response to the regional southward trend of Proto-Gulf extension (Stock and Hodges 1989). The southward progression of extension (basin subsidence) within the Santa Rosalía basin is evident from the restriction of clastic cycles 3 and 4 to the north sub-basin, while cycles 2 to 0 occur in both sub-basins. The inferred relationship between hydrothermal activity and tectonism is consistent with fluid flow models for exhalative deposits (e.g., Lydon 1983, 1984; Sibson et al. 1975; Russell 1983; Goodfellow et al. 1993). On the other hand, fluid flow within stratiform Cu deposits is largely independent of tectonic activity, with some notable exceptions (e.g., Lisbon Valley, White Pine), and is generally the result of dewatering in response to sediment compaction (Kirkham 1989 and references therein). However, compaction-driven flow, likely, did not occur at Boléo, because the maximum compacted statigraphic thickness of the Boléo Formation (~250 m) and of Pliocene to recent sedimentary sequences (~400 m; Wilson and Rocha 1955) would have not been sufficient to generate the pressures (typically 1,500–4,000 m; Kirkham 1989 and references therein) that are necessary to drive the upward migration of basin fluids.

Exhalative discharge is further supported from evidence indicating that basin-wide flow of hydrothermal fluids through the conglomerates was unlikely. The proximity of highly altered, clay facies conglomerate (Figs. 5h, 6h and 11) to fault zones indicates that localized migration of hydrothermal fluids through the conglomerates did occur in the vicinity of basin faults. However, similarities in compositions of least-altered detrital conglomerate and units not associated with highly mineralized mantos (i.e., 0 and 4), with andesite of Sierra San Lucia volcanic rocks (Figs. 5i, 6i and 11), indicate that hydrothermal alteration in conglomerates is minimal. This, in turn, implies that the conglomerates did not serve as aquifers for the hydrothermal fluids. Furthermore, dissimilarities in the Pb isotopic composition (Fig. 12) of bulk sulfide and conglomerates indicate that the residency time of the hydrothermal fluids within the conglomerates was minimal, which is contradictory to fluid flow models for stratiform Cu deposits (Kirkham 1989 and references therein). In regard to the observed enrichment in metals of bulk matrix and assay conglomerate samples, the elevated concentrations in Cu, Co, and Zn are not due to increased abundances of primary sulfides. Rather, these enrichments are due to diagenetic remobilization of metals and precipitation of Cu–Fe–Mn oxides within the upper levels of the conglomerate units.

For downward infiltration of the hydrothermal fluid to have occurred requires that the metal-bearing fluid had the physical properties of a dense (saline) brine. While the fine-grained nature of the mineralization precludes the use of fluid inclusions to constrain the physicochemical behaviour of the fluid, the existence of a saline brine is inferred from the following observations: (1) laminated to bedded sulfide textures (Figs. 5a–c and 6a–c); (2) low temperature of mineralization (this study), which, would require high salinities to transport high quantities of Cu, Co, and Zn (e.g., Sverjensky 1987; Cooke and Large 1998); (3) high sulfate contents of manto sediments (Wilson and Rocha 1955; Conly 2003); and (4) inferred shallow water depths (<200 m; Carreño 1981; Bailes et al. 2001). However, the most decisive evidence for the downward infiltration of metalliferous brine is the stratigraphic distribution of metals within the mantos (Fig. 13). Typically, mantos display a stratigraphic increase in the relative concentration of Zn with respect to Cu and Co (Fig. 13). The enrichment of Cu within the laminated claystone facies and the base of the lowermost breccia unit is interpreted to be the product of chalcocite±covellite replacement of framboidal pyrite (Fig. 6c,d), which precipitated from a brine pool that infiltrated down through the sedimentary pile. The Cu maximum within the lower portion of breccia units (e.g., DDH 610) principally reflects the inclusion of mineralized

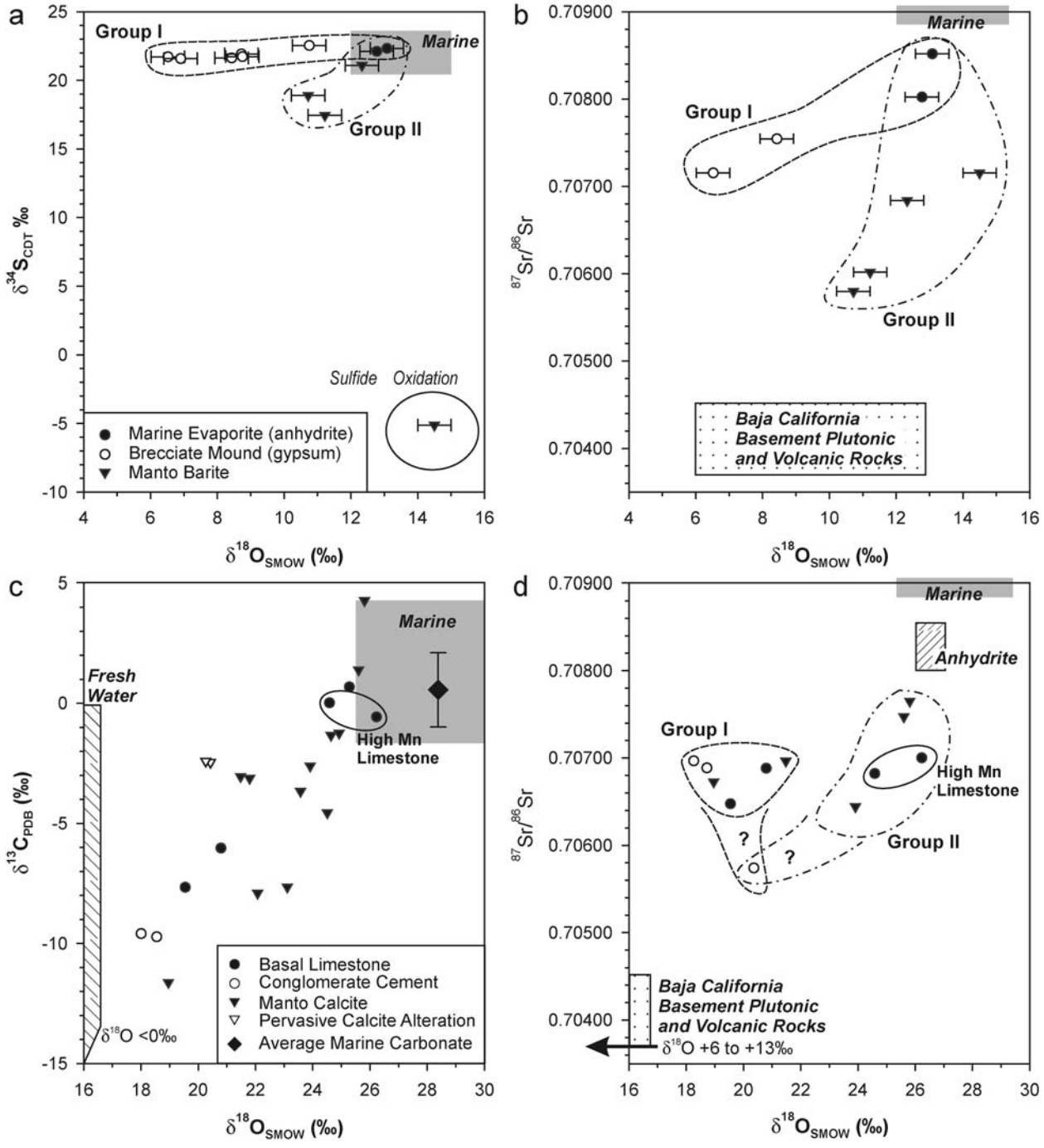

Fig. 7 $\delta^{34}S$ (**a**) and $^{87}Sr/^{86}Srde$ f (**b**) vs $\delta^{18}O$ compositions for Boléo evaporite and hydrothermal sulfate. $\delta^{13}C$ (**c**) and $^{87}Sr/^{86}Sr$ (**d**) vs $\delta^{18}O$ compositions of calcite for Boléo marine, sedimentary and hydrothermal carbonate. $\delta^{34}S$ and $\delta^{18}O$ values for marine sulfate from Claypool et al. (1980). The isotopic composition of marine carbonate, based on $\delta^{18}O$, calculated using the fractionation factors of O'Neil et al. (1969) for calcite-water at 15 to 40°C, and $\delta^{13}C$ for marine mollusks after Keith and Weber (1964). $^{87}Sr/^{86}Sr$ compositions based on the secular curve of Howarth and McArthur (1997) for the 8- to 7-Ma period. Stippled field in graphs **b**,**d** corresponds to $^{87}Sr/^{86}Sr$ and $\delta^{18}O$ composition of Baja crustal rocks ($^{87}Sr/^{86}Sr$ compositions, this study; $\delta^{18}O$ from Taylor and Silver 1978). Cross-hatched field in (c) corresponds to $\delta^{13}C$ of fresh water mollusks (Keith and Weber 1964). Cross-hatched field in (d) corresponds to the range $^{87}Sr/^{86}Sr$ for Boléo-bedded anhydrite

rip-up clasts of laminated claystone (Figs. 5a,b and 6a) that where entrained into the debris flow, and not solely in situ precipitation of sulfides within the breccia matrix. Mineralogical distributions across an individual bed or lamination are also consistent with manto-scale elemental distributions, where Cu sulfides are restricted to the upper portion of pyritic beds/laminations (Fig. 6c). While enrichments in Mn and Zn (±Co±Cu) within the upper laminated claystone facies show that metals were variably remobilized during supergene events, the primary stratigraphic distribution of

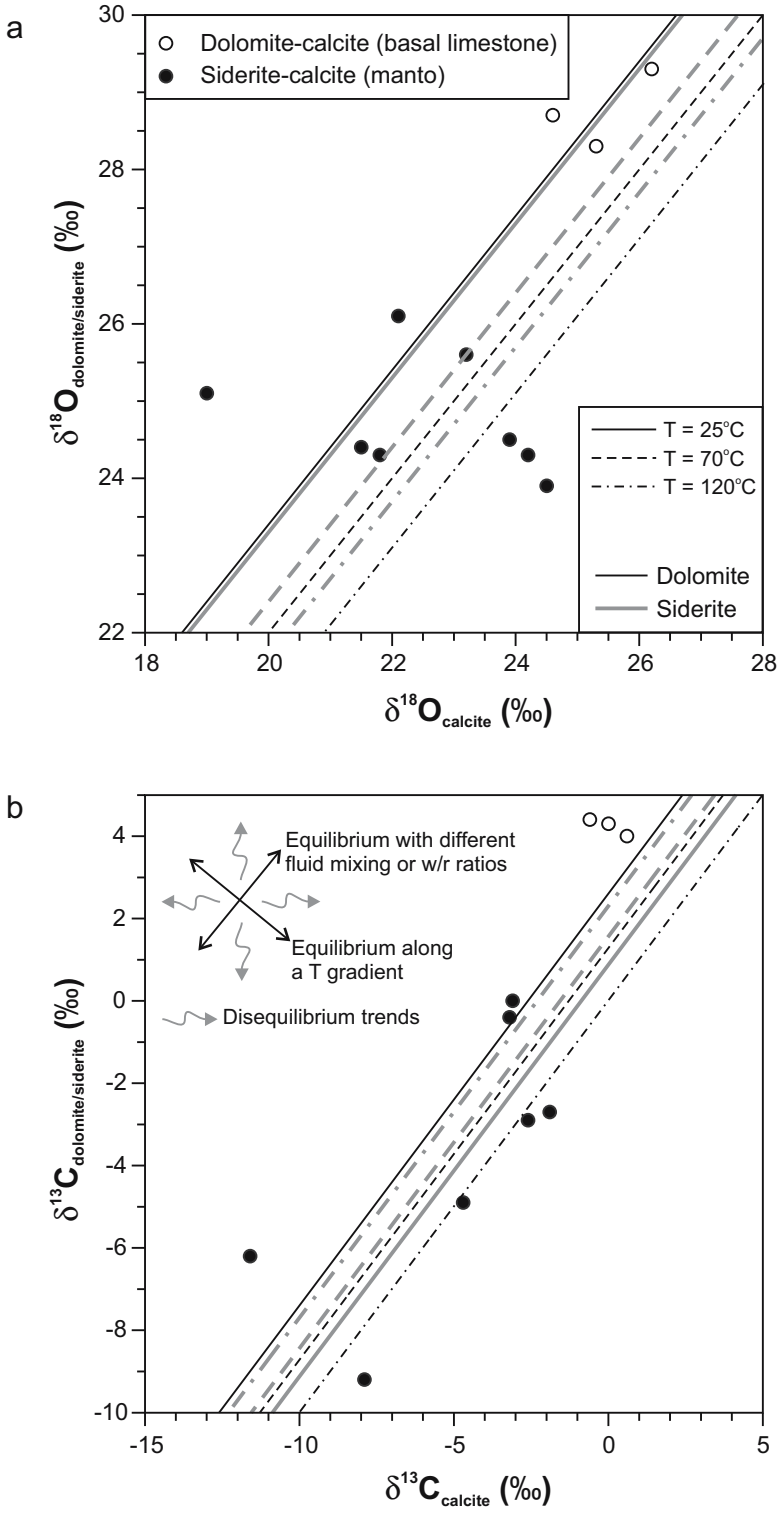

Fig. 8 **a** $\delta^{18}O_{dolomite/siderite}$ vs. $\delta^{18}O_{calcite}$ and **b** $\delta^{13}C_{dolomite/siderite}$ vs. $\delta^{13}C_{calcite}$ equilibrium plots for co-existing carbonate mineral pairs in manto and basal limestone units. Equilibrium is inferred to exist when samples plot either along isotherms, reflecting different fluid-rock ratio or different degrees of fluid mixing, or perpendicular to isotherms, indicating equilibrium along a temperature gradient. Scattering of data or trends oblique to isotherms indicate disequilibrium. Fractionation factors used for $\delta^{18}O$: Ohmoto and Rye (1979) (dolomite); Carothers et al. (1988) (siderite) and O'Neil et al. (1969) (calcite). Fractionation factors used for $\delta^{13}C$: Zheng (1999) (dolomite); Carothers et al. (1988) (siderite) and, Deines et al. (1974)

metals has largely remained intact, as indicated by the similarities in the distribution of metals between sulfide and oxide facies mantos (Fig. 13). The primary elemental and mineralogical distributions are the result of the preferential removal of Cu over Co and Zn from the fluid, due to lower solubilities and higher reaction rates of Cu sulfides arising from fluid interactions with pyrite-bearing laminated claystone (e.g., Sverjensky 1987). The Zn±Co enrichment, as sulphides and primary metalliferous Mn oxides, at higher stratigraphic levels within the breccia facies, is due to entrainment and compaction-driven flow of Cu-depleted residual brine during debris flow incursion.

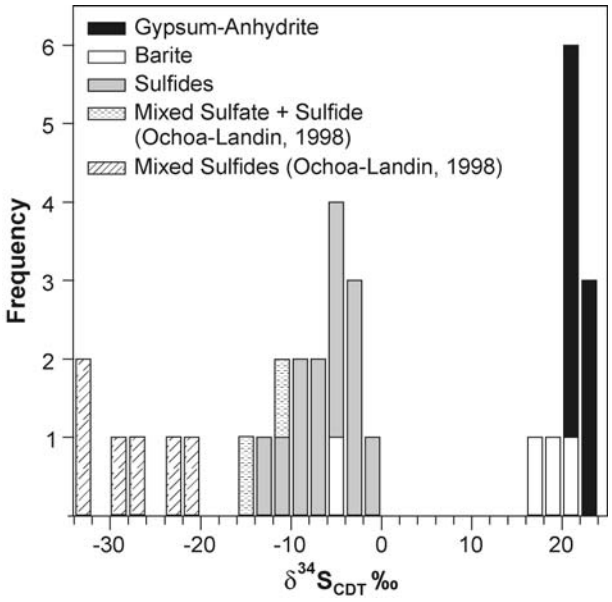

Fig. 9 Histogram showing the distribution of $\delta^{34}S$ values for Boléo sulfides and sulfates

Ambient environment

The Boléo Formation sedimentary rocks were deposited under two distinct sedimentary regimes that record a temporal evolution from shallow brackish-marine carbonates, supported by molluscs of Caribbean and Gulf of California–Pacific affinities (Smith 1991) and evaporites to fluvial-marine prograding fan-deltas. This interpretation is in agreement with earlier studies (e.g., Wilson and Rocha 1955), although more recently, workers interpreted the basal claystone of each cycle to be lacustrine in origin (Ochoa-Landin 1998; Ochoa-Landin et al. 2001).

Marine conditions are inferred from bedded evaporitic anhydrite, which has $\delta^{34}S$ and $\delta^{18}O$ values compatible with precipitation from Miocene seawater (Fig. 7a; Claypool et al. 1980; Ortlieb and Colletta 1984). Strontium isotope ratios of marine evaporite sulfate are lower than expected for Miocene seawater (Howarth and McArthur 1997) and indicate mixing with less radiogenic Sr leached from volcanic and plutonic basement rocks (Fig. 7b) (Taylor and Lasaga 1999). The isotopic composition of gypsum that comprises mound-like structures varies from typical marine values towards lower $\delta^{18}O$ and $^{87}Sr/^{86}Sr$ values, which probably reflects recrystallization due to circulation of meteoric water along reactivated faults during diapir formation.

Surface water input into the Santa Rosalía basin is evident from the covariation among $\delta^{18}O$, $\delta^{13}C$ and $^{87}Sr/^{86}Sr$ of Boléo Formation limestone and conglomerate cements (Fig. 7c,d), which yield mixing arrays between the value for normal marine carbonate and values for surface water carbonate and basement plutonic volcanic rocks. The large range in $\delta^{13}C$ values (0 to −9.7‰) relative to the smaller change in $\delta^{18}O$ (18.6 to 26.2‰) is consistent with surface-water mixing (Allan and Matthews 1982). This interpretation is consistent with the restricted paleogeographic distribution of the basal limestone at the western margin of the Santa Rosalía basin (Wilson and Rocha 1955; Bailes et al. 2001), where mixing with surface water would have been more extensive. Lack of surface-water signature for the evaporites (Fig. 7a,b) and their restriction to the deeper (central) regions of the basin confirm that surface-water input was greater at basin margins. The Tirabuzón Formation limestone has been used to constrain the isotopic composition of mixed fluvial-seawater shoreline water, because it has the lower $\delta^{13}C$ and ^{18}O values, and the least radiogenic $^{87}Sr/^{86}Sr$ ratios and lowest Mn content (0.93 wt%) than of any of the three other limestone samples. Based on the isotopic composition of the Tirabuzón Formation limestone (sample 96-0921-126), shoreline waters are inferred to have been brackish with $\delta^{18}O \approx -9‰, \delta^{13}C_{HCO_3^-} \approx -10‰$ and $^{87}Sr/^{86}Sr \approx 0.7065$ (at 25°C). Although the Tirabuzón Formation limestone is at least one million years younger than the Boléo Formation limestone, isotopic similarity to the least-altered Boléo Formation limestone and calcite cement from Boléo Formation conglomerates imply that it is a reasonable approximation of Santa Rosalía basin shoreline waters.

The Boléo Formation clastic sequence records the stacking of prograding fan–delta cycles (Wilson and Rocha 1955; Ochoa-Landin 1998; Conly 2003) that were deposited under changing conditions from marine to fluvial-marine, corresponding to the gradation from clay stone to conglomerate. This resulted in mixed fluvial-marine isotopic compositions due to the increased input of fluvial water depositing the conglomerates and cross-stratified sandstones. Calcite cement of Boléo Formation fan–delta conglomerate also has $\delta^{13}C$–$\delta^{18}O$ (Fig. 7c) and $^{87}Sr/^{86}Sr$–$\delta^{18}O$ (Group I in Fig. 7d) variations that are consistent with the brackish water trends observed for the basal limestone.

Redox conditions

The change in the ambient environment, from marine to mixed surface or fluvial water-marine, would have produced wide variations in basin redox conditions, which, in turn, influenced sulfide deposition and preservation. Manganese solubility is an effective indicator of redox conditions, where Mn accumulates in anoxic water but is precipitated as oxides under aerated conditions (Cooper et al. 1974; Hirst 1974). The concentration of MnO from drill-hole assays of Boléo Formation sedimentary rocks varies between 0.1 to 0.9 wt% for bulk conglomerate, up to 1.2 wt% for conglomerate matrix, 1.1 to 1.5 wt% for tuffaceous units in the immediate footwall and hanging wall of mantos 2 and 3, and 0.9 to 2.6 wt% for the mantos (Conly 2003). The Mn contents of Boléo Formation clastic sedimentary rocks exceed the average Mn content (0.13 wt%) of black shales deposited in an aerated water column (Quinby-Hunt and Wilde 1994). In addition, Mn nodular crusts at the top of mantos probably represent hydrothermal

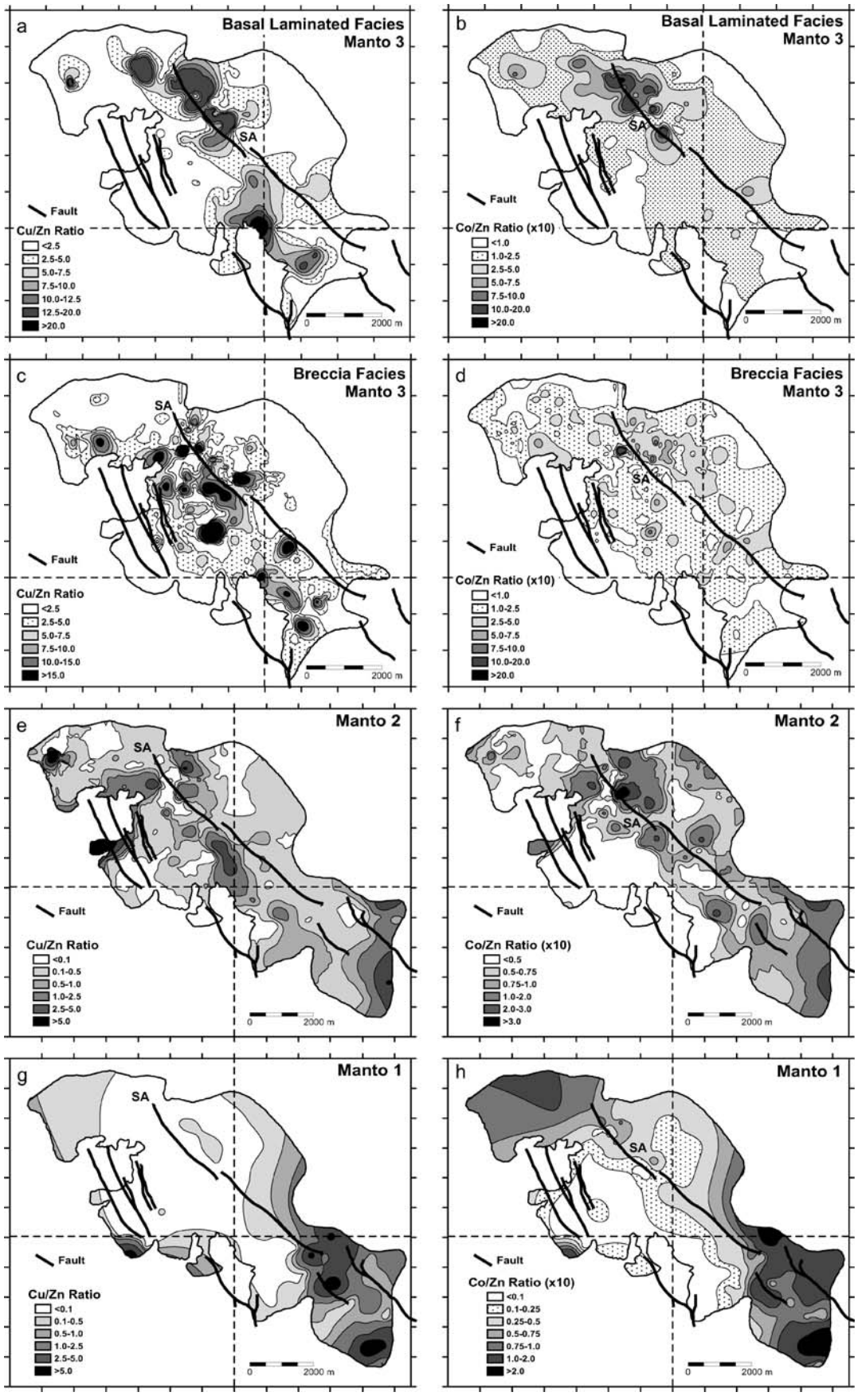
a
Basal Laminated Facies
Manto 3
SA
Fault
Cu/Zn Ratio
<2.5
2.5-5.0
5.0-7.5
7.5-10.0
10.0-12.5
12.5-20.0
>20.0
0
2000 m
b
Basal Laminated Facies
Manto 3
SA
Fault
Co/Zn Ratio (x10)
<1.0
1.0-2.5
2.5-5.0
5.0-7.5
7.5-10.0
10.0-20.0
>20.0
0
2000 m
c
Breccia Facies
Manto 3
SA
Fault
Cu/Zn Ratio
<2.5
2.5-5.0
5.0-7.5
7.5-10.0
10.0-15.0
>15.0
0
2000 m
d
Breccia Facies
Manto 3
SA
Fault
Co/Zn Ratio (x10)
<1.0
1.0-2.5
2.5-5.0
5.0-7.5
7.5-10.0
10.0-20.0
>20.0
0
2000 m
e
Manto 2
SA
Fault
Cu/Zn Ratio
<0.1
0.1-0.5
0.5-1.0
1.0-2.5
2.5-5.0
>5.0
0
2000 m
f
Manto 2
SA
Fault
Co/Zn Ratio (x10)
<0.5
0.5-0.75
0.75-1.0
1.0-2.0
2.0-3.0
>3.0
0
2000 m
g
Manto 1
SA
Fault
Cu/Zn Ratio
<0.1
0.1-0.5
0.5-1.0
1.0-2.5
2.5-5.0
>5.0
0
2000 m
h
Manto 1
SA
Fault
Co/Zn Ratio (x10)
<0.1
0.1-0.25
0.25-0.5
0.5-0.75
0.75-1.0
1.0-2.0
>2.0
0
2000 m

◀ **Fig. 10** Contour diagrams of Cu/Zn and Co/Zn (×10) ratios: **a**, **b** manto 3 laminated facies; **c**, **d** manto 3 breccia facies; **e**, **f** manto 2 (all facies); and **g**, **h** manto 1 (all facies), respectively. Drill-hole assay data courtesy of International Curator Resources. *Grid lines* for 0-north and 0-east and the lateral extent (contouring boundary) of mantos 3–4 and mantos 0–2 (see Fig. 4) are shown for geographic reference. *SA* San Antonio fault

accumulations that formed in an oxygenated water column at the sediment–water interface (Conly 2003).

Fine-grained clastic units and conglomerates with S/C ratios <0.36 were deposited within an oxic water column, whereas, S/C ratios that marginally exceed 0.36 (up to 4.17) indicate moderately reducing conditions (Goldhaber and Kaplan 1974, 1980). Clay and silt units at the base of fan–delta cycles contain variable amounts of framboidal pyrite (Fig. 6b–d), indicating that subsurface reduction was widespread. In conglomerate, S/C ratios greater than 0.36 are not the result of pyrite formation, except for sample 484-173.42, and likely reflect dilution of organic material by terrigenous detritus (Barnes et al. 1990), post-depositional degradation of organic carbon, and/or, increased abundance of authigenic sulfate. Total sulfur content of conglomerates is low, and the sulfide sulfur abundance is generally lower than sulfate sulfur (Table 2). Petrographic observation confirms the low abundance of sulfides in these conglomerates, whereas, sample 484-173.42 contains sulfides indicating reducing conditions during diagenesis or hydrothermal mineralization. The variation in S/C ratios and high sulfate sulfide contents are interpreted to reflect influx of sulfate poor fluvial water (Ohmoto et al. 1990), which is consistent with conglomerate samples (036-82.00 and 429-53.70; Table 3) that are characterized by low $\delta^{13}C$ and $\delta^{18}O$ values.

High S/C ratios (2.07 to 39.40; Table 2) characterize the mantos and are consistent with anoxic conditions arising from either separation of sulfide and organic matter in the water column (Raisewell and Berner 1985; Goodfellow 1987), or decomposition of organic matter in the sedimentary pile (Leventhal 1990; Machel et al. 1995). At Boléo, diagenetic Fe-sulfides are replaced by Cu-sulfides (Fig. 6c,d), with Cu–Co–Zn sulfides filling of intergranular spaces and occurring as finely disseminated grains in the matrix (Fig. 6e,f). The observed sulfide textures, high S/C ratios and the co-existence of sulfides and primary Fe–Mn oxides (Fig. 6e,f) reflect localized sulfate reduction within a predominantly oxygenated sedimentary pile and show that the Santa Rosalía basin water column was non-stratified and oxygenated, thus primarily restricting sulfide formation within the sedimentary pile.

Evolution of the Boléo hydrothermal system

The formation temperature was estimated using the quartz–pyrolusite oxygen isotope geothermometer of Zheng (1991), and ranges from 18 to 118°C (Table 4). The range in temperature is consistent with temperatures inferred from Cu-sulfide-phase equilibria. Monoclinic chalcocite indicates a maximum temperature of 103°C (Roseboom 1966). However, Bailes et al. (2001) reported that chalcocite at Boléo consists of microscopic intergrowths of chalcocite, digenite, and djurleite, which further restricts the temperature between 70 and 93°C (Vaughan and Craig 1978).

The negative sulfur isotope values ($\delta^{34}S<-15‰$) for framboidal pyrite-rich claystone facies reported by Ochoa-Landin (1998) (Fig. 8) are consistent with bacterial sulfate reduction (BSR) of seawater sulfate, with SO_4^{2-}–H_2S fractionation between 55 and 40‰ (Rees 1973; Ohmoto and Rye 1979). The most likely source of dissolved sulfate in uncompacted to partially compacted Boléo manto sediments is seawater trapped in pore spaces or sulfate diffusion after sedimentation. A system open to seawater SO_4^{2-} is consistent with the presence of an oxic water column and soft-sediment deformation features (Fig. 5a)

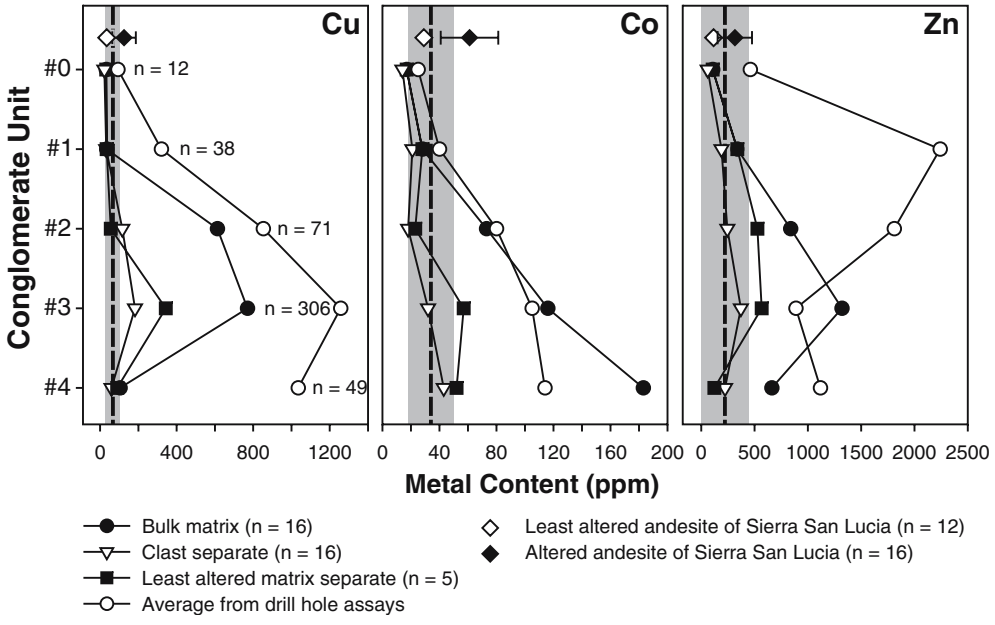

Fig. 11 Stratigraphic variations in Cu, Co and Zn contents of Boléo conglomerate (values in ppm). Average compositions for altered and least-altered arc andesite are shown for comparison (the error bars corresponding to ±1s standard deviation, which for the least-altered andesite is smaller than the symbol). *Dash line* is the calculated composition of the least-altered conglomerate with the *shaded area* equal to the ±1σ error). Drill-hole assay results are courtesy of International Curator Resources

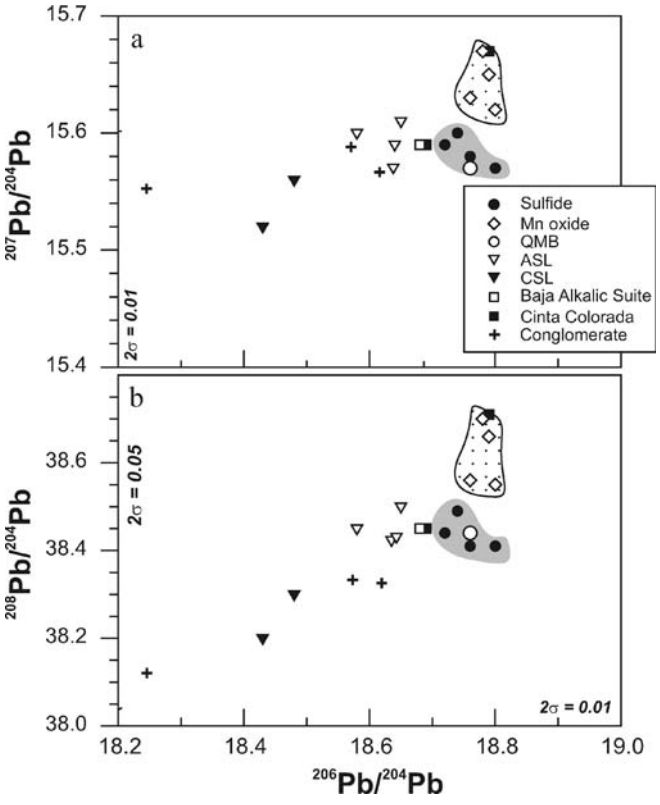

Fig. 12 **a** $^{207/204}$Pb and **b** $^{208/204}$Pb vs $^{206/204}$Pb for Boléo hydrothermal Mn-oxides, sulfides, footwall conglomerates and arc-rift volcanic rocks (from Conly 2003); *CSL* Cerro San Lucas, *ASL* andesite of Sierra San Lucia, *QMB* quartz monzonite basement, *Baja alkalic suite* regional rift-related lavas, *Cinta Colorada* 6.76-Ma tuff that occurs between mantos 2 and 3

that indicate pyrite mineralization to have occurred prior to extensive compaction and dewatering of the sediment. Negative δ^{34}S values (Fig. 9) reflect variable degrees of mixing of light diagenetic pyrite and heavier reduced sulfur associated with Cu–Co–Zn sulfide mineralization. This is, further, supported by the mutual increase in δ^{34}S and Cu/Fe ratio (Fig. 14a), which approximates the relative proportion of Cu sulfides (mainly chalcocite and covellite) to pyrite.

Mixing with pyrite alone cannot account for the variation in sulfur isotopes among Cu–Co–Zn sulfides, because there is a difference in δ^{34}S of up to a 4.2‰ for similar Cu/Fe ratios and Fe contents (Fig. 14a,b). The higher sulfur isotope values (−8.0 to −1.8‰) for Cu–Co–Zn sulfides are consistent with continued bacterial reduction of sulfate under conditions closed or partially closed to SO_4^{2-}. Therefore, the less depleted δ^{34}S values for Cu–Co–Zn sulfide mineralization, likely, represent the addition of isotopically heavy sulfur generated by high-temperature (80–110°C) bacterial sulfate reduction (BSR^{HT}; e.g., Huber et al. 1989; Jørgensen et al. 1992). BSR^{HT} fractionation is poorly constrained; however, BSR^{HT} sulfide from the Guaymas Basin shows a fractionation of ~25‰, which is comparable to the 20 to 36‰ fractionation observed between Boléo sulfate and Cu–Co–Zn sulfides. The need for BSR^{HT} is also indicated by the instantaneous nature of debris-flow sedimentation and occurrence of pre-compaction mineralization (Fig. 5a) that requires geologically instantaneous sulfide production at temperatures up to 118°C, which exceeds the 80°C maximum limit for normal BSR.

Sulfate for BSR was likely pore water/seawater sulfate and/or sulfate transported within the metal-bearing hydrothermal fluids. At the temperature of Boléo mineralization, transport of both sulfur and metals was possible only if sulfur occurred as dissolved sulfate (Sverjensky 1987; Cooke and Large 1998). Low-temperature, sulfate-rich, oxidizing brines may form by dissolution of evaporites by hydrothermal fluids (Sverjensky 1987). Dissolved evaporitic sulfate would have δ^{34}S values equal to the basal Boléo evaporite, because dissolution occurs congruently (Machel et al. 1995; Ohmoto and Rye 1979), and thus would have a sulfur isotope composition identical to that of pore water or seawater sulfate. Dissolution of evaporite is supported texturally by fine-grained gypsum-anhydrite±Fe–Mn oxide± Fe–Cu sulfides that replace primary, coarse-grained evaporitic gypsum (Fig. 6g). Provided that SO_4^{2-}/H_2S disequilibrium was maintained due to slow kinetics and absence of a reducing agent (e.g., carbonaceous matter), the metal-bearing brines could have migrated through the basal evaporite sequence with minimal precipitation of metals (Cooke and Large 1998). Rare pyrite within the basal evaporite implies limited sulfate reduction during either deposition or dissolution of evaporites.

A magmatic source for the sulfur is unlikely because transport of reduced sulfur and metal cations requires fluid temperatures >300°C (Seewald and Seyfried 1990), which greatly exceeds the estimated fluid temperature at Boléo (<120°C). Thermochemical sulfate reduction (TSR) is unlikely because the 20 to 36‰ fractionation between Boléo sulfide and sulfate is beyond the kinetic effect of TSR, where the fractionation decreases from 20 to 10‰ at temperatures from 100 to 200°C (Machel 2001). Furthermore, sulfide generation by TSR is unlikely because reduction rates for TSR are much slower (10^{-6} to 10^{-3} μM·d^{-1}; Machel 1987; Goldhaber and Orr 1995) than BSR^{HT} (19–61 μM d^{-1} of reduced sulfur at Guaymas basin; Jørgensen et al. 1992; Elsgaard et al. 1994).

Sulfide precipitation

The low δ^{34}S values reported by Ochoa-Landin (1998) are consistent with diagenetic pyrite formed by BSR of pore water/seawater sulfate, within the shallow subsurface and/or in a highly restricted anoxic water column via the reaction:

$$2CH_2O_{(\text{organic matter})} + SO_4^{2-}(\text{pore water/seawater}) \rightarrow H_2S + 2HCO_3^- (H_2CO_3 \text{ if pH} < 7) \quad (1)$$

As the Boléo water column was predominately oxygenated, diagenetic pyrite formation would have largely occurred within the shallow subsurface. On the other

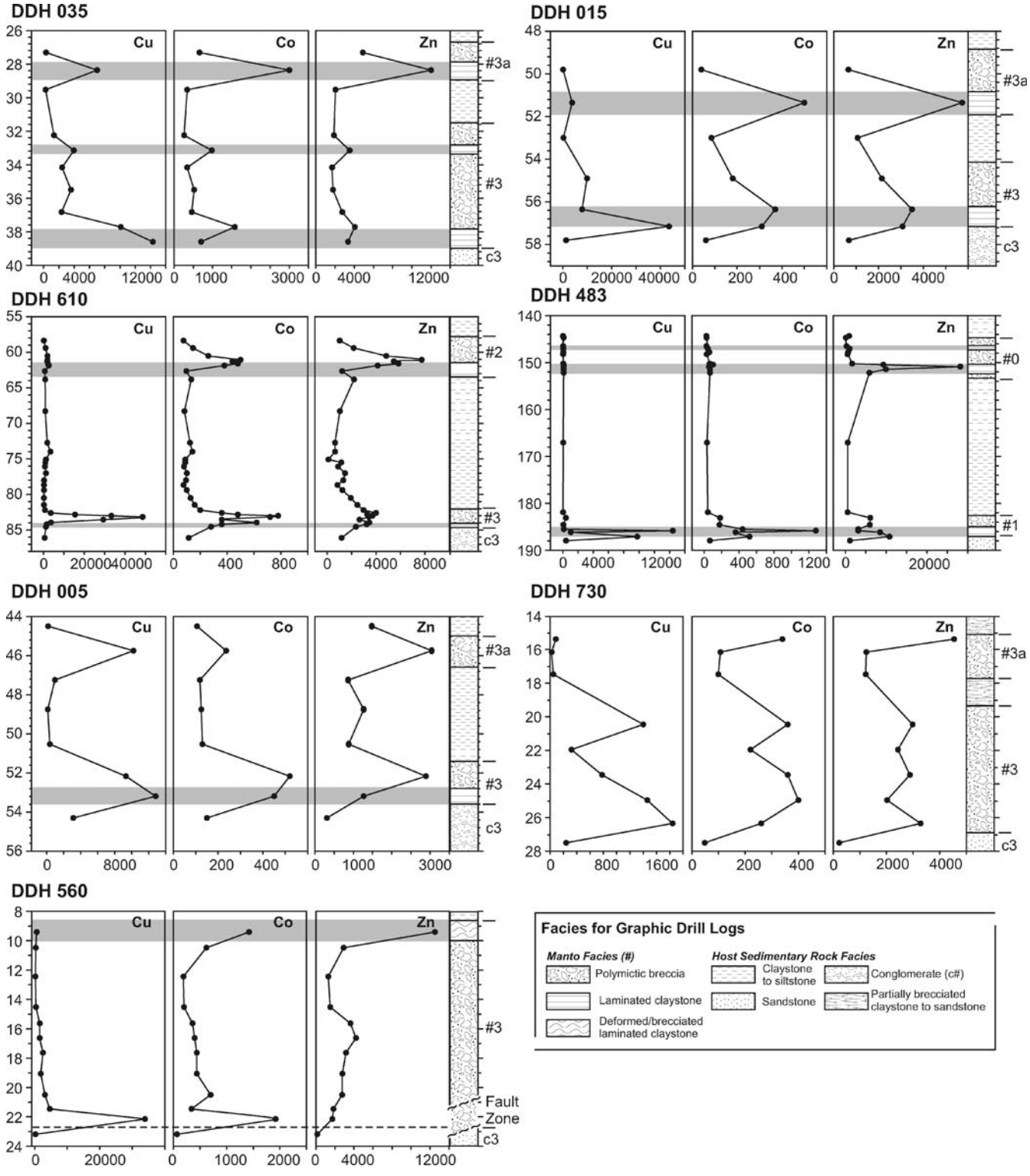

Fig. 13 Representative vertical distributions of Cu, Co and Zn for individual mantos throughout the Boléo Cu–Co–Zn district. Drill-hole collar locations are shown in Fig. 4. Drill holes 005, 015, 035, 483 and 610 intersect sulfide-dominant facies mantos, whereas, drill holes 560 and 730 intersect oxide-dominant facies mantos. Vertical scale is in meters with metal concentration in ppm. Drill-hole assay data courtesy of International Curator Resources. *Shaded bars* correspond to the basal laminated claystone facies of the manto. *Tbcu#* manto, *Tbc#* conglomerate, *Tbt#* claystone to sandstone

hand, laminated claystones with abundant framboidal pyrite (Fig. 6c) may represent the extension of the redox boundary to levels just above the sediment–water interface. Such high pyrite contents would produce a S/C ratio that is significantly greater than 0.36, reflecting separation of pyrite from the residual organic matter by differential sedimentation in the water column (Goodfellow 1987). Framboidal pyrite abundances that exceed 1 to 2 vol% are inconsistent with in situ growth during diagenesis, as the availability of organic matter in fresh marine sediments limits the extent to which sulfate reduction may progress (Goodfellow 1987; Goodfellow, personal communication, 2004). However, the regular influx of oxygenated fluvial waters and debris flows would have spatially and temporally restricted the development of basin anoxia.

The infiltration of oxidizing metalliferious fluids within the sedimentary pile resulted in oxidation of pyrite and liberation of H_2S and SO_4^{2-} by the reaction:

$$2FeS_2 + 3O_2 + 2H_2O \rightarrow 2H_2S + 2Fe^{2+} + 2SO_4^{2-} \quad (2)$$

Liberation of H_2S and the immediate reaction with oxidizing Cu-bearing fluid would have led to the concentric replacement of pyrite framboids following the reaction:

$$2FeS_2 + 4Cu^{+} + 3O_2 + 2H_2O \rightarrow 2Cu_2S + 2Fe^{2+} + 2SO_4^{2-} + 4H^{+} \quad (3)$$

The sulfur isotope composition of the product sulfide and sulfate in reactions 2 and 3 will be similar to that of the parent sulfide (Ochoa-Landin 1998; Ohmoto and Rye 1979). The co-existence of magnetite with pyrite and Cu–Co–Zn sulfides is also consistent with pyrite oxidation (Hanyes 1986; Wilkin and Barnes 1997), according to the reaction:

$$3FeS_2 + 2O_2 \rightarrow Fe_3O_4 + 3S_2 \quad (4)$$

Magnetite-rich samples are characterized by $\delta^{34}S$ intermediate to that of pyrite-rich samples and Cu–Co–Zn sulfides, and reflect either mixing of ^{34}S-depleted remnant pyrite and sulfides precipitated from S_2 from reaction 2 (where $\delta^{34}S_{pyrite} \approx \delta^{34}S_{S2}$) with BSR^{HT} sulfides, or oxidation of both diagenetic pyrite (low $\delta^{34}S$) and BSR^{HT} sulfides (variable $\delta^{34}S$).

To produce the observed range in sulfur isotope composition, ^{34}S-enriched sulfide had to be added to isotopically light pyrite and pyrite-derived H_2S. Isotopically heavy sulfide was added through the filling of sediment porosity by BSR^{HT} hydrothermal Cu–Co–Zn sulfides (Fig. 6e,f). Oxidation rates for pyrite are rapid, ranging from 10^{-10} to 10^{-9} mol m^{-2} s^{-1} (Williamson and Rimstidt 1994; Kamei and Ohmoto 2000), with the amount of H_2S generated being comparable to BSR^{HT}. However, oxidation accounts for only 20 to 30% replacement of framboidal pyrite (Morse 1991). The incomplete consumption of pyrite is supported texturally, where complete replacement of framboids by Cu sulfides is typically only observed for finer-grained framboids (<15 μm; Fig. 6d). Oxidation kinetics may further be inhibited by Fe–Mn oxide and Cu-sulfide armoring of framboids (Morse 1991; Kamei and Ohmoto 2000). For total sulfide abundances of <10 vol%, typical of highly mineralized units at Boléo (Bailes et al. 2001; this study), the contribution of isotopically light pyritic sulfur is small in comparison with the amount of H_2S generated by BSR^{HT}.

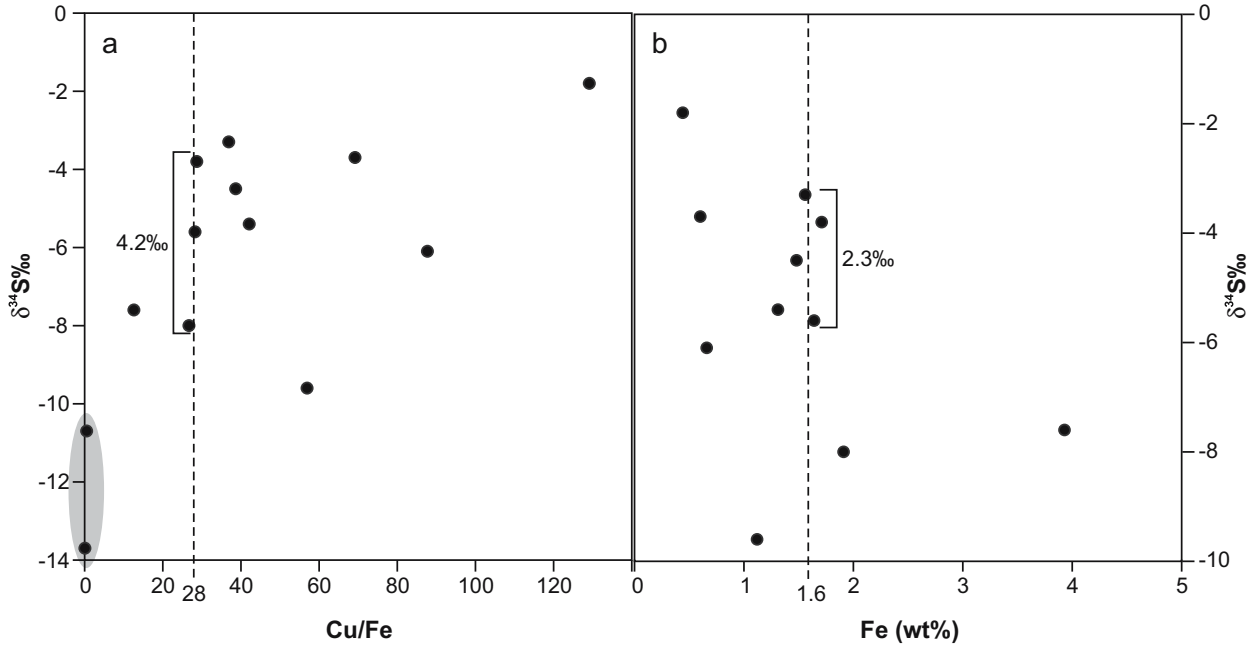

Fig. 14 Variation diagrams of $\delta^{34}S$ and **a** Cu/Fe ratio and **b** total Fe content for manto samples. Metal concentrations obtained by loose powder XRF (data from Conly 2003). *Shaded field* in (a) defines magnetite-rich samples (>40% Fe). *Dashed vertical lines* illustrate variations in $\delta^{34}S$ for similar Cu/Fe ratios and Fe contents

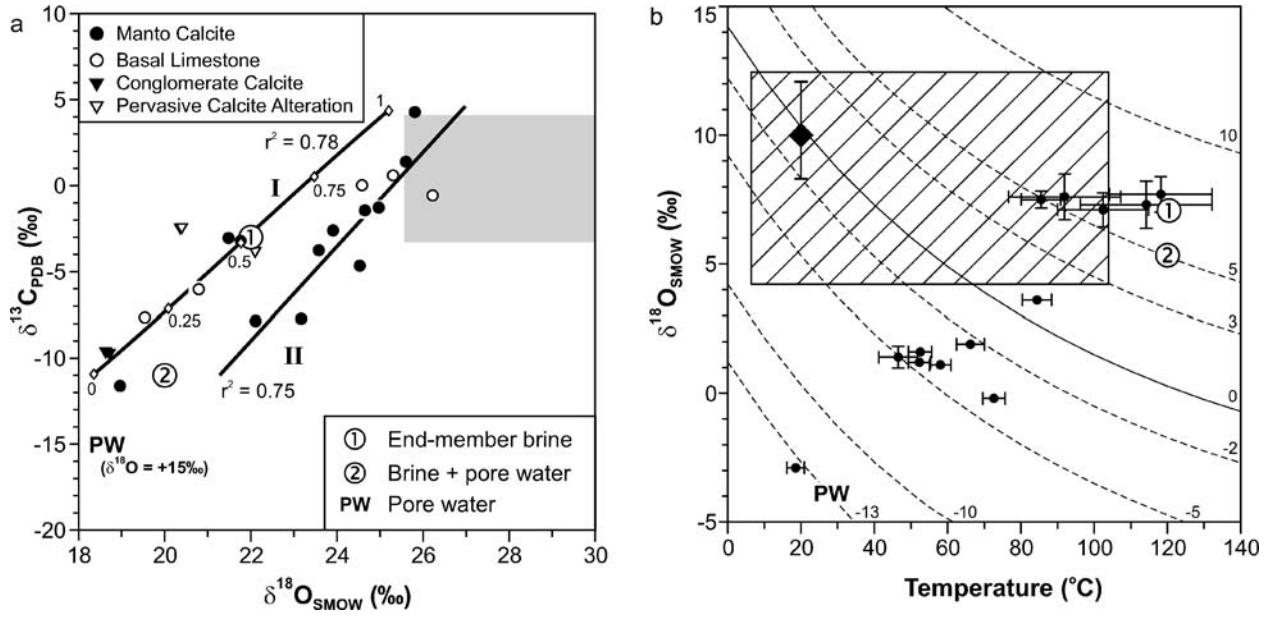

Fig. 15 **a** $\delta^{13}C$ vs $\delta^{18}O$ for Boléo calcite. Calcite values for the basal limestone, conglomerate and cements of volcanic breccias and strata-bound alteration zones are also plotted. *Grey shaded region* is the range in composition of marine calcite precipitated from normal Miocene seawater. *Circles labeled 1 and 2* correspond to calcite (**a**) and brine (**b**) isotopic compositions and temperatures (120°C) of end-member brine and brine that admixed with pore water, respectively (see text). Hydrothermal calcites fall along Trend I. Trend II is the statistically defined water-rock reaction curve for pore water evolution resulting from seawater interacting with Boléo sediment at a constant temperature of 25°C. Mixing proportions along the curve are calculated using the equations of Zheng and Hoefs (1993) and the following parameters: $\delta^{13}C_{seawater}$=+2‰, $^{18}O_{seawater}$=−3‰, $\Delta^{13}C$=−15‰, and $\Delta^{18}O$=−7‰ (where $\Delta = \delta^{initial}_{sediment} - \delta^{final}_{sediment}$). The change in the bulk isotopic composition of the sediment is estimated using the variation values observed for trend II carbonates and clay alteration. The *shaded region* corresponds to the range in $\delta^{13}C$ and $\delta^{18}O$ for marine calcite that precipitated from 25°C seawater. **b** $\delta^{18}O$ vs temperature for Mn oxide mineralization. *Dashed lines* are the $\delta^{18}O$ (‰) compositions of the mineralizing fluid, based on the fractionation factors of Zheng (1991). The *black diamond* represents Mn oxide precipitated from ambient 20°C and 0±2‰ seawater. The *cross-hatched region* shows the range in $\delta^{18}O$ for Boléo Mn oxides that were not in isotopic equilibrium with co-existing silicates

Brine–pore water and brine–sediment interactions

Boléo calcite defines two distinct groups with respect to its C and O isotopic composition (Fig 15a): Group I consists of carbonate cement in coarse-grained clastic units, two samples of manto calcite, least-altered limestone, strata-bound zones of pervasive carbonate mineralization and carbonate-cemented breccias composed of volcanic rock fragments; whereas, Group II consists of manto calcite and high-Mn limestone and representing hydrothermal mineralization.

Group I calcite is largely composed of sedimentary carbonates interpreted to represent seawater (limestone) and pore-water (cement) precipitates. The trends to negative $\delta^{13}C$ and low $\delta^{18}O$ values are not typical of marine carbonates, and are interpreted to reflect seawater mixing with isotopically depleted fresh surface water and/or evolution of pore water during diagenesis. The two manto calcites of this group are interpreted as diagenetic calcites.

Group II hydrothermal carbonates could have formed by several processes: (1) mixing between seawater and brine; (2) calcite precipitation due to brine-sediment interaction; (3) precipitation due to degassing of CO_2; or (4) replacement of primary/diagenetic marine calcite (Zheng 1990; Zheng and Hoefs 1993). Of these four mechanisms, only brine-sediment exchange and replacement of marine calcite can produce the observed range in $\delta^{13}C$ and $\delta^{18}O$ values. Seawater mixing and CO_2 degassing are unlikely because seawater mixing would have been restricted to the upper levels of the brine pool (e.g., LCL of Atlantis II Deep, Red Sea; Turner and Gustafson 1978; Hartmann 1985). Furthermore, boiling of a saline brine with a temperature of 120°C requires a pressure equivalent to a water depth of <10 m (Haas 1971), which is inconsistent with paleo-water depths for the Santa Rosalía basin (~200 m; Carreño 1981; Bailes et al. 2001).

Brine-pore water and brine-sediment interactions during Boléo hydrothermal activity were investigated by applying mass balance models for carbonate mineralization, according to Zheng and Hoefs (1993). For this purpose, $\delta^{13}C$ and $\delta^{18}O$ ratios of +4 and +26‰ at 25°C, respectively, were used for marine calcite, and ratios of −7 and +7‰ at 120°C, respectively, for end-member brine. Isotope fractionation factors for carbon between calcite, HCO_3^- and H_2CO_3 (≈CO_2) were taken from Deines et al. (1974), and for oxygen between calcite and water from O'Neil et al. (1969). The temperature and $\delta^{18}O$ of the end-member brine correspond to the silicate-corrected oxygen isotope values for high-temperature Mn oxides (Fig. 15b) and Mn oxide–water fractionation from Zheng (1991). We were unable to quantify the $\delta^{13}C$ value of the brine and, therefore, as an approximation, used the median value for Guaymas Basin and Escanaba Trough vent fluid CO_2 (Shanks et al. 1995).

The lowest $\delta^{13}C$ and $\delta^{18}O$ values for calcite could not be modeled by the dissolution–replacement of diagenetic marine calcite by end-member brine. To produce highly depleted manto calcite, the mineralizing brine would have had $\delta^{13}C$ values of approximately −15‰ and $\delta^{18}O$ values of approximately +5‰ at 120°C. The light isotopic brine composition, likely, is a result of mixing with pore water that was isotopically depleted by diagenetic reactions involving organic matter (Sass et al. 1991), diagenetic carbonate precipitation (Irwin et al. 1977; Mozley and Burns 1993) and/or the transformation of volcanic ash to smectite (Pirrie and Marshal 1991; Morad and De Ros 1994). Pore water compositions are constrained by the minimum isotopic compositions of sedimentary calcite and Mn oxide (Fig. 15). Interaction with seawater-derived pore fluid is supported by the positive correlation between $^{87}Sr/^{86}Sr$ and $\delta^{18}O$ for manto calcite (Fig. 7d). The shift by −2 and −8‰ in $\delta^{18}O$ and $\delta^{13}C$, respectively, between mixed pore water–brine and the initial end-member brine indicates a 20 to 30% dilution by end-member pore water with a $\delta^{18}O$ of approximately −13 to −10‰ and $\delta^{13}C$ of approximately −15 to −12‰. Pore water–brine mixing is a result of the downward infiltration of brine into the sedimentary pile. As discussed earlier, the downward infiltration of brine is inferred from the stratigraphic distribution of metals within the mantos (Fig. 13) and from the highly localized occurrence of pervasive alteration within conglomerate units, which indicates that lateral fluid flow through permeable horizons was minimal. The observed range in isotope compositions of Boléo calcite is reproducible by the dissolution–recrystallization of diagenetic marine calcite by brine mixed with pore water over a temperature range of 100 to 60°C and water–rock ratios of 10:1 to 0.5:1 (Fig. 16). The positive correlation between $\delta^{13}C$ and $\delta^{18}O$ records decreasing water–rock ratios and conductive cooling within the sediments.

The change in the isotopic composition of calcite arises from the presence of two carbonate reactants in the dissolution reaction:

$$CaCO_{3(\text{marine calcite})} + H_2CO_{3(\text{fluid})} \leftrightarrow 2HCO_3^- + Ca^{2+} \quad (5)$$

Carbonic acid (H_2CO_3) was either transported in the brine or generated as a reaction product of BSR (Eq. 1; Anderson and Garven 1987). Marine calcite would have an isotopic composition along Group I in Fig. 7b, whereas aqueous carbonate is depleted in ^{13}C due its derivation from organic matter. $\delta^{13}C$ values of hydrothermal calcite decrease with increasing water–sediment ratio due to the greater proportion of BSR-generated carbonic acid to marine calcite. The extent to which BSR drives calcite dissolution is dependent on the proximity of sulfide deposition to H_2S generation (Anderson and Garven 1987) and buffering by the surrounding rock/sediment (Machel 2001). The redox state of the Boléo sedimentary pile would have readily oxidized reduced species, and, in turn, would have restricted sulfide deposition to the site of H_2S generation to provoke dissolution of marine carbonate (Anderson and Garven 1987). Co-precipitation of sulfide and carbonate in this environment requires the system to be buffered by fluid–silicate reactions (Anderson and Garven 1987), which is

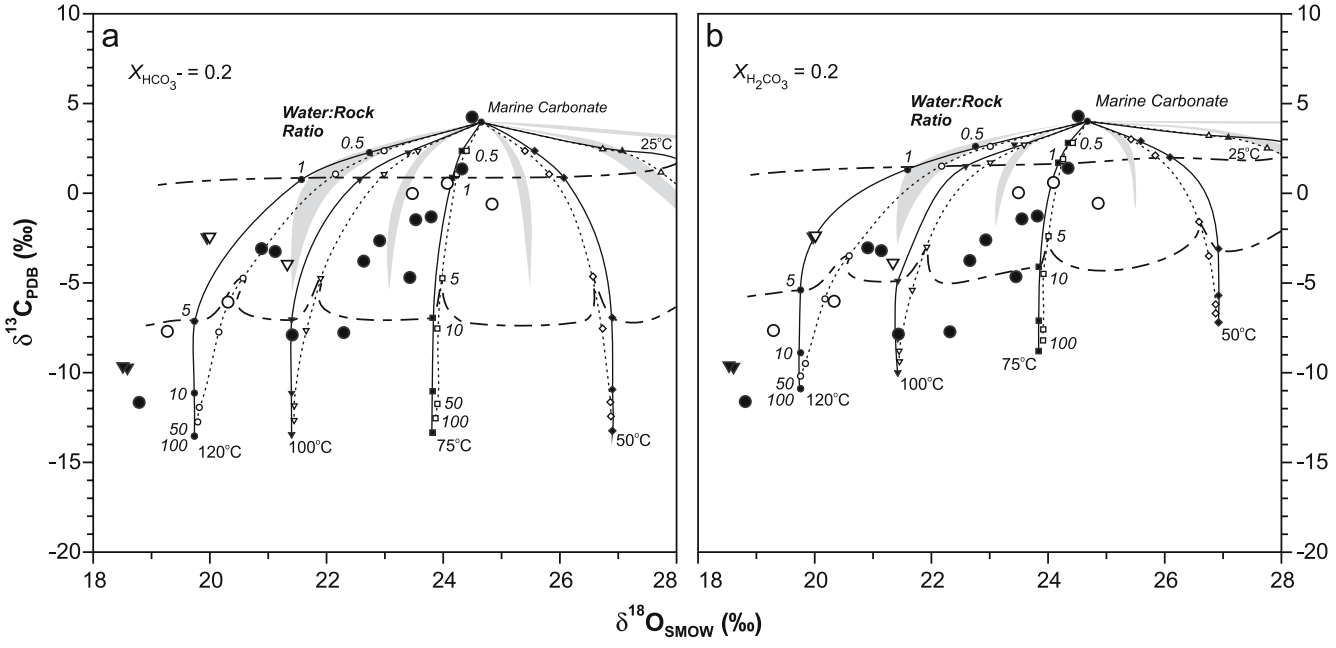

Fig. 16 Carbon and oxygen isotope variations of calcite precipitated in response to alteration of primary marine calcite by **a** HCO_3^- and **b** H_2CO_3 dominant brine at progressively increasing brine:rock ratios, for fluids with a mole fraction of 0.2 for the carbonate species. *Shaded fields* correspond to calcite alteration by end-member brine, and the *solid and dashed black lines* correspond to brine that admixed with pore water prior to interaction with carbonate (see text). *Solid curves* denote an open system and *dashed curves* denote a closed system. Data symbols same as in Fig. 15

consistent with diagenetic and hydrothermal alteration of volcanic ash to smectite at Boléo (Wilson and Rocha 1955; Bailes et al. 2001; Ochoa-Landin et al. 2001).

Conclusion

The following conclusions pertaining to the genesis of the Boléo Cu–Co–Zn mineralization can be drawn from this study:

(1) The chemical nature of Miocene-age Santa Rosalía basin water is strongly controlled by paleogeography. Near-shore limestone has $\delta^{13}C$ and $\delta^{18}O$ values controlled by mixing ambient seawater and fluvial water, whereas, distal and deeper water evaporite units have isotopic signatures characteristic of Miocene seawater. Strontium isotopes are less radiogenic and indicate modification of basin seawater due to interaction with volcanic rocks.

(2) Low S/C ratios, elevated Mn contents, and sedimentological evidence indicate that the basin water column was oxidizing. The oxygenated basin-restricted sulfide precipitation within the sedimentary pile resulted in the replacement of early diagenetic framboidal pyrite and filling of pore space by Cu–Co–Zn sulfides. Local anoxic conditions within the sedimentary pile are supported by high S/C ratios of mantos.

(3) Oxygen isotope geothermometry of quartz–Mn oxides yields a mineralization temperature of <118°C, which is consistent with the occurrence of chalcocite, the dominant Cu-sulfide.

(4) Negative $\delta^{34}S$ values (<−20‰) for pyrite-rich units imply that diagenetic pyrite sulfur originated from bacterial sulfate reduction at ambient temperatures within the sedimentary pile. Increased $\delta^{34}S$ values that approach 0‰ for Cu–Co–Zn sulfide mineralization indicate the occurrence of high-temperature (>80°C) bacterial sulfate reduction within the sedimentary pile during the infiltration of the metal-bearing brines. BSR^{HT}-generated sulfide occurs as rim replacements of framboidal pyrite and as open-space fillings within the matrix of the manto breccias.

(5) Quantitative C–O isotope modeling indicates that hydrothermal manto calcite formed as the result of dissolution and replacement of authigenic marine calcite by downward infiltrating metalliferous brine, which, prior to reaction with calcite, admixed with isotopically depleted pore water.

(6) A conventional red bed model is inconsistent with many of the Boléo's unique geological characteristics (e.g., mineralization rip-up fragments within the breccias). Rather, an exhalative-infiltration model, similar to Sangster's (2002) model for disseminated mineralization along the periphery of SEDEX deposits, is proposed to describe the nature of hydrothermal fluid flow, where: (1) up-flow and discharge onto the basin floor of saline metalliferous brines occurred along basin growth faults; (2) mineralization of the basal claystone is the product of downward infiltration of brine, which is best supported from the vertical distribution of metals within the mantos, through the shallow sedimentary pile, resulting in the replacement of diagenetic pyrite; and (3) portions of the mineralized claystone were subsequently eroded and entrained into debris flows, with mineralization of debris-flow breccia deposits due to continual hydrothermal activity. Apart from localized supergene remobilization, disruption in the overall stratigraphic trend in metal content of the mantos corresponds to the stacking of multiple debris flows, where three sharp increases in metal grade within laminated claystone beds (Fig. 13) at higher stratigraphic levels reflect the infiltration of newly discharged brine.

Acknowledgements This research was funded through Natural Sciences and Engineering Research Council (NSERC) of Canada research grants and an Industrially Oriented Research grant to S.D. Scott. Additional support was provided to A. Conly through an NSERC Post-Graduate Scholarship and two H.E. McKinstry Student Research Grants from the Society of Economic Geologists. We thank the geological staff of International Curator Resources for their logistical support in the field and financial assistance to the project. Mike Gorton (University of Toronto), Brian Cousens (Carleton University) and Kerry Klassen (Queen's University) are thanked for their assistance with whole-rock analysis, strontium isotope analyses and BrF_5 oxygen isotope extraction, respectively. Numerous suggestions for improvements were made on earlier versions of this manuscript by Adrian Boyce, Murray Hitzman, Hartwig Frimmel and an anonymous reviewer.

References

Allan JR, Matthews RK (1982) Isotopic signatures associated with early meteoric diagenesis: Sedimentology 29:797–817

Anderson GM, Garven G (1987) Sulfate–sulfide–carbonate associations in Mississippi Valley-type lead–zinc deposits. Econ Geol 82:482–488

Atwater T (1989) Plate tectonic history, northeastern Pacific and western North America. In: Winterer EL, Hussong DM, Decker RW (eds) The eastern Pacific Ocean and Hawaii. The Geology of North America. Geol Soc Am Bull, N:21–72

Bailes RJ, Christoffersen JC, Escandon VF, Peatfield GR (2001) Sediment-hosted deposits of the Boléo copper–cobalt–zinc district, Baja California Sur, Mexico. Soc Econ Geol (Spec Publ) 8:291–306

Bar-Matthews M, Matthews A (1990) Chemical and stable isotope fraction in manganese oxide-phosphorite mineralization, Timna Valley, Israel. Geol Mag 127:1–12

Barnes MA, Barnes WC, Bustin RM (1990) Chemistry and diagenesis of organic matter in sediments and fossil fuels. In: McIlreath IA, Morrow DW (eds) Diagenesis. Geosci Can (Reprint Series 4), Geological Association of Canada, pp 189–204

Blair TC, Bilodeau WL (1988) Development of tectonic cyclothems in rift, pull-apart and foreland basins: sedimentary response to episodic tectonism. Geology 16:517–520

Carothers WW, Adami LH, Rosenbauer RJ (1988) Experimental oxygen isotope fractionation between siderite-water and phosphoric acid liberated CO_2-siderite. Geochim Cosmochim Acta 52:2445–2450

Carreño AL (1981) Ostracodes y foraminiferos planctonicos de la loma del Tirabuzon, Santa Rosalía, Baja California Sur, e implicaciones bioestratigraficas y paleoecologicas. Universidad Nacional Autónoma de México, Instituto de Geologica Revista 5:55–64

Claypool CE, Holser WT, Saki IR, Zak I (1980) The age curves for sulfur and oxygen isotopes in marine sulfate and their mutual interpretation. Chem Geol 28:199–260

Clayton RN, Mayeda TK (1963) The use of bromine pentafluoride in the extraction of oxygen from oxides and silicates for isotopic analyses. Geochim Cosmochim Acta 27:43–52

Conly AG (2003) Origin of the Boleo Cu–Co–Zn deposit, Baja California Sur, Mexico: implications for the interaction of magmatic-hydrothermal fluids in a low-temperature hydrothermal system. Unpublished Ph.D. thesis, University of Toronto, Toronto, p 433

Conly AG, Brenan JM, Bellon H, Scott SD (2005) Arc to rift transitional volcanism in the Santa Rosalía region, Baja California Sur, Mexico. J Volcanol Geotherm Res 142:303–341

Cooke DR, Large RR (1998) Practical uses of chemical modelling—defining new exploration targets in sedimentary basin. J Aust geol geophys 17:259–275

Cooper JR, Daasch EJ, Kaye M (1974) Isotope and elemental geochemistry of Black Sea sediments. In: Degens ET, Ross DA (eds) The Black Sea. Am Assoc Petr Geol Bull Mem 20:554–565

Cousens BL (1996) Magmatic evolution of Quaternary mafic magmas at Long Valley Caldera and the Devils Postpile, California: Effects of crustal contamination on lithospheric mantle-derived magmas. J Geophys Res 101, no. B12:27,673–27,689

Curray JR, Moore DG (1984) Geologic history of the mouth of the Gulf of California. In: Crouch JK, Bachman SB (eds) Tectonics and sedimentation along the California margin. Pacific Section, SEPM 38:17–39

Deines P, Langmuir D, Harmon RS (1974) Stable carbon isotope ratios and the existence of a gas phase in the evolution of carbonate ground waters. Geochim Cosmochim Acta 38:1147–1164

Elsgaard L, Isaksen MF, Jørgensen BB, Alayse AM, Jannasch HW (1994) Microbial sulfate reduction in deep-sea sediments at the Guaymas Basin hydrothermal vent area: influence of temperatures and substrates. Geochim Cosmochim Acta 58:3335–3343

Friedman I, O'Neil JR (1977) Compilation of stable fractionation factors of geochemical interest. In: Fleischer M, (ed) Data of geochemistry. US Geological Survey professional paper, 440–KK, p 12

Gastil RGD, Phillips RP, Allison EC (1975) Reconnaissance geology of the state of Baja California. Geol Soc Am Bull Mem 140:170

Goldhaber MD, Kaplan IR (1974) The sulfur cycle. In: Goldberg ED (ed) The Sea, vol 5, Marine Chemistry. Wiley, New York, pp 303–336

Goldhaber MD, Kaplan IR (1980) Mechanisms of sulphur incorporation and isotope fractionation during early diagenesis in sediments of the Gulf of California. Mar Chem 9:95–143

Goldhaber MD, Orr WL (1995) Kinetic controls on thermochemical sulfate reduction as a source of sedimentary H_2S. In: Vairavamurthy MA, Schoonen MAA (eds) Geochemical transformations of sedimentary sulfur. Am Chem Soc Monogr, ACS symposium series 612:412–425

Goodfellow WD (1987) Anoxic stratified oceans as a source of sulphur in sediment-hosted stratiform Zn–Pb deposits (Selwyn Basin, Yukon, Canada). Chem Geol 65:359–382

Goodfellow WD, Lydon JW, Turner RJW (1993) Geology and genesis of stratiform sediment-hosted (SEDEX) zinc–lead–silver sulphide deposits. In: Kirkham RV, Sinclair WD, Thorpe RI, Duke JM (eds) Mineral deposit modeling. Geol Assoc Can (special paper) 40:201–251

Haas JL Jr (1971) The effect of salinity on the maximum thermal gradient of a hydrothermal system at hydrostatic pressure. Econ Geol 66:940–946

Hanyes DW (1986) Stratiform copper deposits hosted by low-energy sediments: I. Timing of sulfide precipitation—a hypothesis. Econ Geol 81:250–265

Hartmann M (1985) Atlantis-II Deep geothermal brine system. Chemical processes between hydrothermal brines and Red Sea deep water. Mar Geol 64:157–177

Hirst DM (1974) Geochemistry from eleven Black Sea cores. In: Degens ET, Ross DA (eds) The Black Sea. Am Assoc Petr Geol Mem 20:430–455

Holt JW, Holt EW, Stock JM (2000) An age constraint on Gulf of California rifting from the Santa Rosalía basin, Baja California Sur, Mexico. Geol Soc Amer Bull 112:540–549

Howarth RJ, McArthur JM (1997) Statistics for strontium isotope stratigraphy. A robust LOWESS fit to the marine Sr-isotope curve for 0–206 Ma, with look-up table for the derivation of numerical age. J Geol 105:441–456

Huber R, Kurr M, Jannasch HW, Stetter KO (1989) A novel group of abyssal methanogenic archaebacteria (*Methanopyrus*) growing at 110°C. Nature 342:833–834

Irwin H, Curtis C, Coleman M (1977) Isotopic evidence for source of diagenetic carbonates formed during burial of organic-rich sediments. Nature 269:209–213

Jørgensen BB, Isaksen MF, Jannasch HW (1992) Bacterial sulfate reduction above 100°C in deep-sea hydrothermal vent sediments. Science 258:1756–1757

Kamei G, Ohmoto H (2000) The kinetics of reactions between pyrite and O_2-bearing water revealed from in situ monitoring of DO, Eh and pH in a closed system. Geochim Cosmochim Acta 64:2585–2601

Karig DE, Jensky W (1972) The protogulf of California. Earth Planet Sci Lett 17:169–172

Keith ML, Weber JN (1964) Isotopic composition and environmental classification of selected limestones and fossils. Geochim Cosmochim Acta 28:1787–1816

Kirkham RV (1989) The distribution, settings and genesis of sediment-hosted stratiform copper deposits. In: Boyle RW, Brown AC, Jefferson CW, Jowett EC, Kirkham RV (eds) Sediment-hosted stratiform copper deposits. Geol Assoc Can (Special paper) 36:3–38

Kornexl BE, Gehre M, Höfling R, Werner RA (1999) On-line $\delta^{18}O$ measurement of organic and inorganic substances. Rapid Commun Mass Spectrom 13:1685–1693

Larson RL (1972) Bathymetric, magnetic anomalies, and plate tectonic history of the mouth of the Gulf of California. Geol Soc Am Bull 83:3345–3360

Ledesma-Vázquez J, Johnson ME, Romero-Rios F (1999) Evolución tectónica del Golfo de California: Mioceno–Plioceno de Bahía Concepción, BCS: Gaceta de la Asociación Mexicana de Geólogos Petroleros 3:1–5

Lonsdale P (1989) Geology and tectonic history of the Gulf of California. In: Winterer EL, Hussong DM, Decker RW (eds) The eastern Pacific ocean and Hawaii. The Geology of North America, vol N. Geological Society of America, pp 499–522

Leventhal JS (1990) Organic matter and thermochemical sulfate reduction in the Viburnum Trend, Southeast Missouri. Econ Geol 85:622–632

Lydon JW (1983) Chemical parameters controlling the origin and deposition of sediment-hosted stratiform lead–zinc–silver deposits. In: Sangster DF (ed) Short course in sediment-hosted stratiform lead–zinc deposits. Mineralogical Association of Canada, Short course handbook 8:175–250

Lydon JW (1984) Volcanogenic massive sulphide deposits. Part I: A descriptive model. Geosci Can 11:195–202

Machel HG (1987) Some aspects of diagenetic sulphate–hydrocarbon redox reactions. In: Marshall JD (ed) Diagenesis of sedimentary sequences. Geol Soc Spec Publ 36:15–28

Machel HG (2001) Bacterial and thermochemical sulfate reduction in diagenetic settings—old and new insights. Sediment Geol 140:143–175

Machel HG, Krouse HR, Sassen R (1995) Products and distinguishing criteria of bacterial and thermochemical sulfate reduction. Appl Geochem 10:373–389

McCrea JM (1950) On the isotope chemistry of carbonates and a palaeotemperature scale. J Chem Phys 18:849–857

Morad S, De Ros LF (1994) Geochemistry and diagenesis of stratabound calcite cement layers within the Rannoch Formation of the Brent Group, Murchison Field, North Viking Graben (northern North Sea)—comment. Sediment Geol 93:135–141

Morse JW (1991) Oxidation kinetics of sedimentary pyrite in seawater. Geochim Cosmochim Acta 55:3665–3667

Mozley PS, Burns SJ (1993) Oxygen and carbon isotopic composition of marine carbonate concretions: an overview. J Sediment Petrol 63:73–83

Ochoa-Landin L (1998) Geological, sedimentological and geochemical studies of the Boléo Cu–Co–Zn deposit, Santa Rosalía, Baja California, Mexico. Unpublished Ph.D. thesis, University of Arizona, Tucson, p 148

Ochoa-Landin L, Ruiz J, Calmus T, Perez E, Escandon F (2001) Sedimentology and stratigraphy of the upper Miocene Boleo Formation, Santa Rosalía, Baja California, Mexico. Rev Mex cienc geol 17:83–95

Ohmoto H, Rye RO (1979) Isotopes of sulfur and carbon. In: Barnes HL (ed) Geochemistry of hydrothermal ore deposits, 2nd edn: Wiley, New York, pp 509–567

Ohmoto H, Kaiser CJ, Geer KA (1990) Systematics of sulphur isotopes in recent marine sediments and ancient sediment-hosted base metal deposits. Proceedings of the Conference on Stable Isotopes and Fluid Processes in Mineralization, Queensland, Australia, pp 70–120

O'Neil JR, Clayton RN, Mayeda TK (1969) Oxygen isotope fractionation in divalent metal carbonates. J Chem Phys 51: 5547–5558

Ortlieb L, Colletta B (1984) Sintesis cronoestratigrafica sobre el Neogeno y el Cuaternario marino de la cuenca Santa Rosalía, Baja California Sur, Mexico: Neotectonics and sea level variations in the Gulf of California area. Universidad Nacional Autónoma de México, Instituto de Geologica Revista 8:241–260

Pirrie D, Marshal JD (1991) Field relationships and stable isotope geochemistry of concretions from James Ross Island, Antarctica. Sediment Geol 71:137–150

Pufahl PK, Fralick PW (2004) Depositional controls on Paleoproterozoic iron formation accumulation, Gogebic Range, Lake Superior region, USA. Sedimentology 51:791–808

Quinby-Hunt MS, Wilde P (1994) Thermodynamic zonation in the black shales facies based on iron–manganese–vanadium content. Chem Geol 113:297–317

Raisewell R, Berner RA (1985) Pyrite formation in euxinic and semi-euxinic sediments. Am J Sci 285:710–724

Rees CE (1973) A steady-state model for sulphur isotope fractionation in bacterial reduction processes. Geochim Cosmochim Acta 37:1141–1162

Roseboom EH (1966) An investigation of the system Cu–S and some natural copper sulfides between 25 and 700°C. Econ Geol 61:64–672

Rosenbaum J, Sheppard SM, (1986) An isotopic study of siderites, dolomites and ankerites at high temperatures. Geochim Cosmochim Acta 50:1147–1150

Russell MJ (1983) Major sediment-hosted exhalative zinc + lead deposits: Formation from hydrothermal convection that deepen during crustal extension. In: Sangster DF (ed) Short course in sediment-hosted stratiform lead–zinc deposits. Mineralogical Association of Canada (Short-course handbook) 8:251–282

Sangster DF (2002) The role of dense brines in the formation of vent-distal sedimentary-exhalative (SEDEX) lead–zinc deposits: field and laboratory evidence. Miner Depos 37:149–157

Sass E, Bein A, Almogi-Labin A (1991) Oxygen-isotope composition of diagenetic calcite in organic-rich rocks: evidence for ^{18}O depletion in marine anaerobic pore water. Geology 19:839–842

Sawlan MG, Smith JG (1984) Petrologic characteristics, age and tectonic setting of Neogene volcanic rocks in northern Baja California Sur, Mexico. In: Frizzell VA Jr (ed) Geology of the Baja California Peninsula. Pacific Section, SEPM 39:237–251

Seewald JS, Seyfried WE Jr (1990) The effect of temperature on metal mobility in subseafloor hydrothermal systems: constraints from basalt alteration experiments. Earth Planet Sci Lett 101:388–403

Shanks WC III, Böhlke JK, Seal RR (1995) Stable isotopes in mid-ocean ridge hydrothermal systems: interactions between fluids, minerals, and organisms. In: Humphris SE, Zierenberg RA, Mullineau LS, and Thomson RE (eds) Seafloor hydrothermal systems: physical, chemical, biological, and geological interactions. American Geophysical Union, Geophys Monogr 91, pp 194–221

Sharma T, Clayton RN (1965) Measurement of $^{18}O/^{16}O$ ratios of total oxygen of carbonates. Geochim Cosmochim Acta 29: 1347–1353

Sibson RH, Moore JM, Rankin AH (1975) Seismic pumping—a hydrothermal fluid transport mechanism. J Geol Soc (Lond) 131:653–659

Smith JT (1991) Cenozoic marine mollusks and paleogeography of the Gulf of California. In: Dauphin JP, Simoneit BRT (eds) The Gulf and Peninsular province of Californias. Am Assoc Petr Geol Mem 47, pp 301–369

Stock JM, Hodges KV (1989) Pre-Pliocene extension around the Gulf of California and the transfer of Baja California to the Pacific Plate. Tectonics 8:99–115

Steel RJ, Maehle S, Nilsen H, Røe SL, Spinnangr Å (1977) Coarsening-upward cycles in the alluvium of Hornelen Basin (Devonian) Norway: sedimentary response to tectonic events. Geol Soc Am Bull 88:1124–1134

Stock JM, Lee J (1994) Do microplates in subduction zones leave a geological record? Tectonics 13:1472–1487

Sverjensky DA (1987) The role of migrating oil field brines in the formation of sediment-hosted Cu-rich deposits. Econ Geol 82:1130–1141

Taylor AS, Lasaga AC (1999) The role of basalt weathering in the Sr isotope budget of the oceans. Chem Geol 161:199–214

Taylor HP, Silver LT (1978) Oxygen isotope relationships in plutonic igneous rocks in the northern 600 km of the Cretaceous Peninsular Ranges Batholith, southern and Baja California. Geol Soc Am Bull (Abstracts with programs) 10:503

Touwaide ME (1930) Origin of the Boleo copper deposit, Lower California, Mexico. Econ Geol 25:113–144

Turner JS, Gustafson IH (1978) The flow of hot saline solutions from vents in the sea floor—some implications for exhalative massive sulfide and other ore depsits. Econ Geol 73:1082–1100

Vaughan DJ, Craig JR (1978) Mineral chemistry of metal sulfides. Cambridge University Press, Cambridge, p 493

Veizer J, Fritz P (1976) Possible controls of post-depositional alteration in oxygen paleotemperature determinations. Earth Planet Sci Lett 33:255–260

Wilkin RT, Barnes HL (1997) Formation processes of framboidal pyrite. Geochim Cosmochim Acta 61:323–339

Williamson MA, Rimstidt JD (1994) The kinetics and electrochemical rate-determining step of aqueous pyrite oxidation. Geochim Cosmochim Acta 58:5443–5454

Wilson IF, Rocha VS (1955) Geology and mineral deposits of the Boléo Copper District Baja California, Mexico. US Geol Surv prof pap 273:134

Zheng Y-F (1990) Carbon–oxygen isotopic covariation in hydrothermal calcite during degassing of CO_2. A quantitative evaluation and application to the Kushikino gold mining area in Japan. Mineralium Deposita 25:246–250

Zheng Y-F (1991) Calculation of oxygen isotope fractionation in metal oxides. Geochim Cosmochim Acta 55:2299–2307

Zheng Y-F (1999) Oxygen isotope fractionation in carbonate and sulfate minerals. Geochem J 33:109–126

Zheng Y-F, Hoefs J (1993) Carbon and oxygen isotopic covariations in hydrothermal calcites. Theoretical modeling on mixing processes and application to Pb–Zn deposits in the Harz Mountains, Germany. Mineralium Deposita 28:79–89